A cleaner and more efficient energy system achieving a sustainable future for road transport

Nan Zhang, Yiji Lu [*], Zhibin Yu [1]

James Watt School of Engineering, University of Glasgow, Glasgow, G12 8QQ, UK

ARTICLE INFO

ABSTRACT

A novel integrated cooling system is developed for future medium to large electric vehicles by integrating the fuel cell, battery, metal-hydride, heat pump, and liquid desiccant dehumidification system to reduce power consumption and extend vehicle's driving range. The system benefits from the reuse of the normally wasted energy in the form of pressure difference and wasted thermal energy, from the hydrogen vessel, the fuel cell stack, and the battery pack. A numerical model for the proposed system and a finite element model for the dehumidifier and regenerator are developed and validated by experimental results from published data. A comprehensive evaluation of the impacts of the ambient air temperature and humidity, fuel cell current output, battery discharging C rate, and air mass flow rate on the Coefficient of Performance (COP), outlet air temperature, and cooling capacity is conducted. Two operating modes, namely non-compressive mode and heat pump supplemental mode are investigated and a detailed comparison between these two modes is undertaken. Furthermore, the proposed system under heat pump supplemental mode has been compared to other published cooling systems and dehumidification systems. Under non-compressive mode, results indicate that the proposed system can provide sufficient cooling capacity without the need of the compressor when the supply air mass flow rate is lower than 0.03 kg/s, under the specific operating situation. Under the heat pump supplemental mode, the proposed system can operate at 36 °C with a COP greater than 4, which is 56% higher than the cited published results, although the COP of the proposed system also considers battery cooling. Heat pump supplemental mode drastically reduces the 12-s insufficient cooling period that occurs at the beginning of the charging to discharging transition between the two metal hydrides to 2 s compared to non-compressed mode. Overall, this study provides a potential solution for future zero-emission vehicles by utilizing the heat and electric co-generation characteristic of the fuel cell, the isothermal characteristic of the metal hydride, and dehumidification and cooling characteristics of the liquid desiccant dehumidification system to extend the driving range of the electric vehicles and reduce energy consumption for cooling. Moreover, the proposed system can also provide domestic cooling loads and power by integrating the system into residential buildings.

1. Introduction

After COP26, there has been a global focus on limiting global warming to +1.5 °C compared to the pre-industrial era. However, the progress still falls short of the previous goal of controlling warming to under +2 °C (COP 26 in Glasgow, 2021). Hence, all governments now acknowledge the necessity of reducing the use of fossil fuels to reduce Greenhouse Gas (GHG) emissions. In the EU, road transport is heavily dependent on fossil fuels and accounts for 22% GHG emissions (Robaina and Neves, 2021). As a result, vehicle decarbonization through electrification has been worldly recognised as the future development tendency for the transport sector in order to reduce GHG emissions by 40% by 2030. However, the shift to electric vehicles has been slower than expected, especially in Europe and the United States, which account for only 20% of global EV sales in total (Crabtree, 2019). One of the main reasons for the slow implementation of electric vehicles is driving range anxiety. Additionally, the energy consumption caused by the HVAC system in EVs cannot be neglected. Different from traditional Internal Combustion Engine (ICE) vehicles, the HVAC system in EVs is not only responsible for cooling the cabin in summer but also plays a key role in the vehicle's thermal management system, such as keeping

Nomenclature

Symbols

A	area [cm^2] for fuel cell [m^2] for heat exchanger
Ac	circulation area [m^2]
Cv	EEV flow coefficient
Cp	specific heat capacity [J/(kg K)]
d_h	hydraulic diameter [m]
D	mass diffusivity [m/s]
D_f	fractal dimension
E	entropy [J/kgK]
f	fanning friction factor
F	Faraday's constant 96485 [coulombs/mol]
h	heat transfer coefficient [W/m2/K]
H	enthalpy [J/kg]
i_{fg}	enthalpy of vaporization [J/kg]
I	current[A]
K_m	Overall mass transfer coefficient [m/s]
l	thickness [cm]
$\dot{m}$	Mass flow rate [kg/s]
M	molecular weight [kg/mol]
Me	Metal
N(n)	Number of cells
P	partial pressure [atm]
Pr	Prandtl number
Q	heat [W]
R	universal gas constant 8.31447 [kPa·m3/(kmol·K)]
Re	Reynolds number
t	time [s]
T	temperature [K]
U_h	Overall heat transfer coefficient [W/m^2/K]
v	velocity [m/s]
V	voltage [V]
W	energy consumption [W]
w	hydrogen capacity [%]
X	vapour quality

Greek symbol

ρ	density [kg/m^3]
μ	dynamic viscosity [Pa·s]
ε	porosity
λ	heat conductivity [W/m·K]
β	inclination angle
ω	specific humidity [kg/kg]
σ	membrane thickness [m]
φ	packing fraction

Subscripts

act	activation loss
ach	airflow channel
amb	ambient
bat	battery
cell	single fuel cell
ch	battery charging
chi	chiller
comp	compressor
con	concentration loss
cond	condenser
dch	battery discharging
de	dehumidification
des	desorption
eff	effective
eva	evaporator
eq	equivalent
FC	fuel cell
hp	heat pump
H_2	Hydrogen
i	inner
irr	irreversible
lq	liquid
m	mean
max	maximum
min	minimum
nernst	nernst open circuit
o	outer
ohm	ohmic losses
OC	open circuit
ref	refrigerant
rev	reversible
s	solid
sol	solution
SP	separate plate
vp	vapour
w	water

Abbreviations

COP	coefficient of performance
DR	Driving range
EEV	electronic expansion valve
EV	electrical vehicle
FC	Fuel Cell
GHG	greenhouse gas
GWP	global warming potential
HP	heat pump
HVAC	heating, ventilation, and air conditioning
ICE	internal combustion engine
LMTD	logarithmic mean temperature difference
MH	metal hydride
MPC	model predictive control
PEMFC	proton-exchange membrane fuel cell
PID	proportion-integral-derivative
RH	relative humidity [%]
SOC	state of charge

battery and electrical devices within their optimal operating conditions.

The average energy consumption for cabin cooling ranges from 2000W to 4000W when the ambient temperature ranges from 30 °C to 50 °C (Bridge et al., 2013). The peak transient energy consumption for the HVAC system can reach 7800W at mid-day in summer (Kambly and Bradley, 2014). Recently, research about the performance of EVs' HVAC systems has largely focused on the performance of low Global Warming Potential (GWP) refrigerants and advanced control logic as the structure and logic of the HVAC in EVs for cabin comfort as there is no significant difference compared to that in ICE vehicles. Xie et al. (2022) proposed a two-layered control strategy and compared it to the conventional rule based controllers, for example. The results show that the developed control strategy can improve energy consumption by 30.2% and 12.4% respectively compared to the on-off controller and proportion-integral-derivative (PID) controller. Meng et al. (2018) evaluated the performance of the R1234yf/R134a mixture when applied to an automotive air conditioning system. The results indicate that the adopted mixture can provide a similar cooling capacity but with a lower COP compared to using pure R134a refrigerant and the GWP is higher than the pure R1234yf. Fang et al. (2021) evaluated the cooling

performance of a mobile transcritical CO_2 air conditioning system with an internal exchanger. The proposed system could provide cooling capacity up to 4500W and the COP was 1.7, which is lower than the current widely adopted refrigerant R134a air conditioning system. Therefore, with increasingly strict refrigerant GWP regulations and the usage of low GWP refrigerants, the energy consumption for cabin comfort in summer will increase. The inhomogeneity of the temperature field in the cabin when using a traditional automobile HVAC system is huge, especially at the air outlet of the air conditioner. This is because of the dehumidification characteristics of the traditional air conditioner, the temperature must reach the dew point temperature, which is far lower than the set temperature of the cabin. This cold air can blow directly on the driver and passengers and cause discomfort. Normally, a pre-heater is installed before the air outlet to compensate for the deep cooling process in traditional air conditioning systems (Zhang et al., 2019a). Alahmer et al. (Alahmer, 2016) introduced an evaporative desiccant cooling and dehumidification system to the vehicle air conditioning system and achieved a COP of 0.7–0.9 due to the required heat for regeneration, but the COP would be 3.5 to 4.5 if waste heat can be utilized. However, the proposed system by Alahmer et al. has some drawbacks, including an increase in weight due to the water tank. Membrane-based liquid desiccant dehumidification is an alternative to evaporative desiccant cooling and dehumidification system which can provide dehumidification and cooling together but omit the evaporate cooling process. Chen et al., 2018, 2019 investigated the performance of the KCOOH cross flow membrane based liquid desiccant air conditioning system. The results indicated a good air moisture removal rate and a certain degree of cooling effect. However, the system's cooling effect is highly dependent on the operating temperature of the solution. And the massive heat requirement for solution regeneration makes it hard to be applied to vehicles. For fuel cell vehicles, with the traditional air conditioning, only the cabin thermal management would cause a reduction of driving range by 17.3% under New York urban driving cycle when the ambient temperature is 35 °C (Wu et al., 2022).Considering the battery pack and cabin thermal management together, Deng et al. (2023) designed an integrated system thermal management for plug-in fuel cell electric vehicle with an implementation of the soft actor-critic algorithm. They conducted that 28.12% or even more energy was consumed by the prolonged operation of air conditioning system. Farsi et al. (Farsi and Rosen, 2022) proposed an integrated air-based thermal management system for PEMFC-assisted battery electric vehicles in cold weather. The cold air entering the battery pack not only can keep the battery temperature but also can be supplied to the fuel cell. The fuel cell efficiency could be improved by 3% when the supplied was preheated from 10 °C to 40 °C. Similarly, Xu et al. (2020) also built an integrated system for fuel cells and battery thermal management system for hot weather at 40 °C degree. The supplied air for the fuel cell was pre-heated by a motor, air compressor, and other electronic components. But the battery pack was still cooled down by the traditional AC system. The results only demonstrated the feasibility of the system but did not mention the efficiency and energy consumption of the system. However, neither Farsi's nor Xu's integrated systems considered the cabin thermal management together. Although Li et al. (2023) built a vehicle thermal management system for cabin comfort by using waste heat from the fuel cell and battery packs, they only considered using the waste heat for heating mode and no improvement for cooling performance. They concluded that 505.68g H_2 was consumed by the proposed cooling system when the ambient temperature was 34 °C. To further reduce the cooling energy consumption in summer, metal-hydride cooling systems have recently drawn the transport sector's attention as a replacement for the traditional automobile air conditioning system (Vashisht and Rakshit, 2021). However, currently, most of the studies focus on applying the hydrogen storage characteristics to the fuel cell vehicle (Lototskyy et al., 2020; Davids et al., 2019) and integrated with fuel cell to provide required heat for the desorption of the metal hydride. Few studies tried to utilise its thermal characteristics for cooling. Di Giorgio et al. (Di

Giorgio et al., 2022) introduced a new battery thermal management system by integrating it with metal hydride tank for fuel cell hybrid electric vehicles. The proposed system can successfully reduce the battery temperature by 15 °C. Meier et al. (2018) introduced a metal hydride based cooling system for electric vehicle with a fuel cell range extender. They predicted that the proposed system has the potential to reduce the impact of the sensible heat to around 15% resulting in a cooling power of 21% of the generated electricity with specific mass ratio. Weckerle et al. (2019a) developed an open-metal-hydride system with an integrated a fuel cell in order to utilise the energy waste during the pressure drop between the H_2 supply procedure from hydrogen vessel to the fuel cell stack. The experimental results revealed that the system can provide 276 kW/MH$_{(kg)}$ while providing 7 kW electric power. However, the performance of the proposed system was affected by the temperature difference between absorption and desorption temperature. Thermal loss occurs when the two metal hydrides work alternately, resulting in a 17% loss of cooling capacity within one cycle, even showing negative effects in the first 20 s of the cycle (Weckerle et al., 2019b).

However, unlike the ICE vehicle, cabin thermal comfort in zero-emission vehicles cannot be considered separate from the battery and other electronic devices. Hence, the integrated thermal management system for zero-emission vehicles in summer attracts the attention of researchers.

Ma et al. (2022) experimentally studied the performance of the integrated thermal management system for pure electric vehicles. They emphasized that vehicle level thermal management is necessary from the battery safety perspective even at normal operating conditions. However, that movement would impose more work on HVAC system and require the use of an additional 10.34kWh more energy compared to separate cooling systems. Xu et al. (Xu and Arjmandzadeh, 2023) studied the range impact of a vehicle level thermal management system which integrated battery coolant and cabin air system together with a refrigerant loop. The proposed model was built based on the parameters of the Tesla model S and model 3. The results demonstrated that the EV range was reduced by 38%–45%. Zou et al. (2014) investigated the performance of an air conditioning system coupling with battery cooling. They demonstrated that with the increasing ambient temperature, more energy will be consumed. Consequently, when the battery output was 0.3C (350W) and 0.8C (850W) the air conditioning system required 42.5% and 18.8% of the total battery capacity. This means, for urban operating conditions, the air conditioning system will consume a significant amount of battery capacity. It should be noted that Zou et al. highlighted the potential utilisation of battery waste heat to pre-heat the deep cooling supply air and recommended that it should be further investigated. Gillet et al. (2018) investigated a multi-evaporator and chiller air conditioning and battery cooling system. A COP of 3.88 and a cooling capacity of 7650W could be achieved when the battery cooling loop was deactivated. However, with the increase in battery cooling demands, the front evaporator tended to be insufficient due to the predominance of the chiller side. This arrangement will sacrifice the cabin's thermal comfort to some extent. Although increasing the total refrigerant mass flow rate could solve the problem, the energy consumption for thermal comfort will increase correspondingly.

Overall, the current HVAC based vehicle thermal management system for zero-emission vehicles can require up to 45% battery capacity in hot climates and the value would be much higher with the promotion of low GWP refrigerants and the desire for high-level cabin thermal comfort. Liquid desiccant dehumidification is a good alternative method to avoid deep cooling, increase the thermal comfort level, and supply more fresh air. But the heat required for solution regeneration and how to manage it from a vehicle perspective needs further investigation. Metal hydride cooling systems attract significant attention because of their clean and non-compressing cycle. However, few studies focus on the cooling performance of metal hydride integrated cooling systems for zero-emission vehicles and the duration of cooling load fluctuations at

the beginning of the metal hydrides' transitions from absorption to desorption is long when the cooling load is only provided by the metal hydride system. Moreover, the size of the metal hydrides limited by the cooling power-to-weight ratio is also a main barrier to implementing a metal hydride system. Although some scholars have tried to improve thermal management performance by building an integrated system, the wasted energy has not been fully utilized, and the deduction of driving range is still significant.

In this context, to provide stable cooling capacity to cabin, battery, and electronic devices and increase the cabin thermal comfort level but eliminate the driving range deduction, a metal hydride-assisted, heat pump supplement liquid desiccant thermal management system for an electric vehicle with a fuel cell backup is proposed in this study. An open-metal-hydride system is designed between the hydrogen vessel and fuel cell stack to provide cooling effects to the liquid desiccant. A liquid desiccant system with a low-temperature solution is adopted to cool and dehumidify the air to the set point. A heat pump utilises the waste heat for solution regeneration and also works as a supplement for the system. The proposed system has two operating modes in this study which are the non-compressing mode and heat pump supplement mode. Numerical modes for two separating modes are developed in MATLAB and validated based on experimental or published results. At the end of the study, the performance of these two operating modes is evaluated in detail and compared with conventional systems in terms of COP and cooling capacity.

The key innovation of this work is by proposing an integrated system that can provide cooling effects removing the normal dependence on the vapour compression system meeting the cooling requirements of cabin cooling, battery cooling, electronics cooling, and high-level thermal comfort, contributing to the technological development of new cooling energy system for the electric vehicle. In the proposed system, the deep cooling process is not needed, the COP is higher compared to the tradition Air Conditioning System. And the temperature fluctuation can be shortened to improve thermal comfort and efficiency. Furthermore, with the supplement of the heat pump air conditioning system, the proposed system could limit the size of the open metal hydride system. Moreover, the proposed system not only can be used for onboard

vehicles supporting the development of Future Zero Emission vehicles but will also be of interest for domestic cooling and electricity cogeneration.

2. System description

In Fig. 1, the working principle of the proposed fuel cell and open metal-hydride based, heat pump assisted liquid desiccant cooling, dehumidification and regeneration system for FCBEV is illustrated. The proposed system contains four subsystems which are an open hydride cooling system, fuel cell and battery energy system, heat pump, and liquid desiccant cooling, dehumidification and regeneration system. Among them, the open metal-hydride cooling system and fuel cell and battery energy system are depicted in Fig. 2 while the heat pump and liquid desiccant cooling, dehumidification and regeneration system are shown in Fig. 1. The liquid desiccant, after the desiccant cooler (port 12), flows through the open metal-hydride cooling system to acquire cooling loads. If the temperature of the liquid desiccant meets the set point at the exit of the open metal-hydride cooling system, the liquid desiccant can be pumped to a hollow fibre dehumidifier to process the cabin inlet air directly. However, if the cooling loads provided by the open metal-hydride are not enough, the liquid desiccant should pass by the evaporator first before entering the hollow fibre dehumidifier in order to release heat to the refrigerant side of the heat pump system. The outlet liquid desiccant from the hollow fibre dehumidifier is split into two streams, the main one flows through the condenser to extract heat while the other one enters the inter cooler for the fuel cell coolant loop to absorb heat when the waste heat from the battery pack is insufficient for regeneration. The high temperature liquid at port 9 undergoes a heat and mass transfer procedure with ambient air in the hollow fibre regenerator in order to reach the set concentration and then flows through the desiccant cooler if further cooling is required. In the heat pump subsystem, a traditional cycle containing a chiller, evaporator, accumulator, compressor, condenser, and electric expansion valve (EEV) is utilized. Refrigerant enters the chiller from port 23 aiming to absorb the waste heat from the battery pack and fuel cell stack (optional). The status of the refrigerant at the outlet of the chiller is
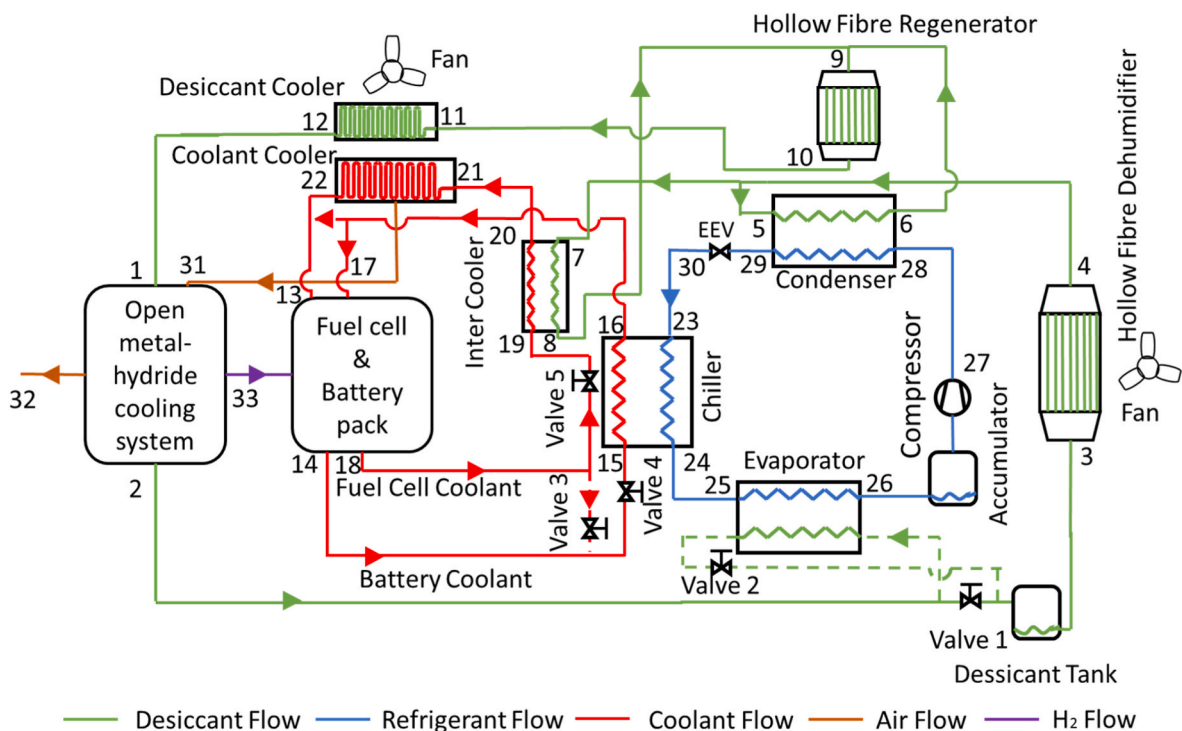
Fig. 1. Schematic diagram of the proposed system.
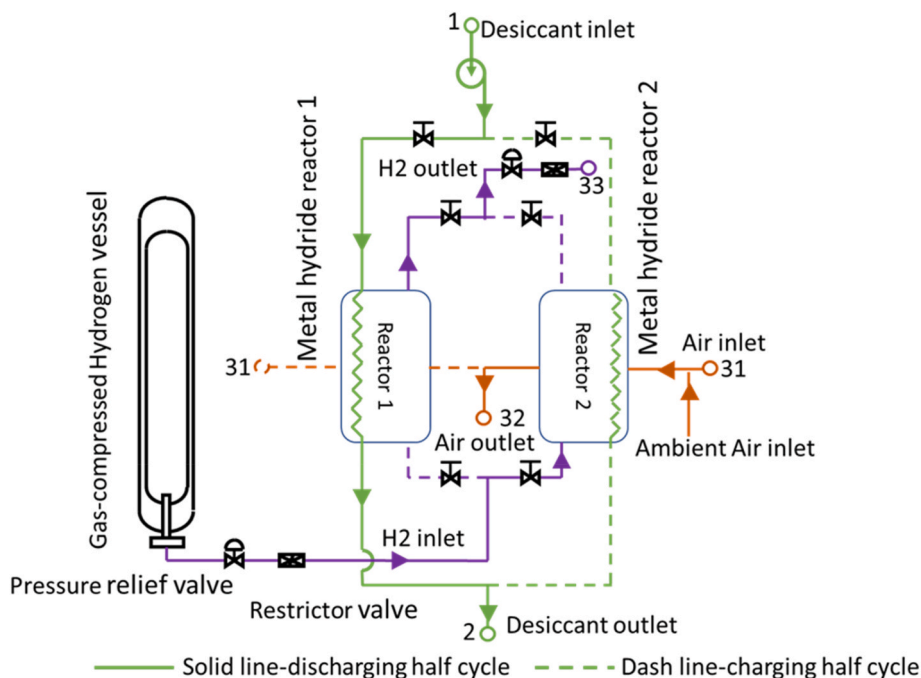
Fig. 2. Schematic diagram of the subsystem using the open metal-hydride.

controlled by the evaporator. If the evaporator is operating, the refrigerant at the outlet of the chiller is in a mixed state, otherwise, it is in a superheated vapour state. After being compressed by the compressor, the hot and high-pressure vapour refrigerant releases the waste heat to the desiccant side and is then throttled by the EEV and the cycle is finished. For the fuel cell and battery coolant side, the fuel cell coolant and battery coolant flow out of the subsystem in parallel. The battery coolant flows along route 14-15-16-17. However, the fuel cell coolant has two streams. The mainstream flows along 18-19-20-21-22-13 while the bypass flows along 18-15-16-13. In the mainstream, the fuel cell coolant first passes the inter-cooler to be initially cooled down by the low-temperature desiccant and then flows past the coolant cooler to further reduce the coolant temperature to the set point by using ambient air. It should be mentioned that the bypass can only be accessed when the desiccant temperature for regeneration is not sufficient. The air flow across the coolant cooler will be utilized in the open metal-hydride cooling system.

The schematic diagram of the open metal-hydride subsystem is shown in Fig. 2. In the middle of the onboard H_2 transportation between the gas-compressed hydrogen vessel and fuel cell stack, two metal hydride reactors are applied to utilise the energy waste during the hydrogen de-pressure procedure. The subsystem can be divided into two half cycles, namely a discharging half cycle and a charging half cycle shown as solid and dashed lines respectively. For the charging half cycle, the hydrogen supplied by the gas-compressed hydrogen vessel first relieves its pressure to the required operating status of metal hydrides by passing the pressure relief valve and restrictor valve. The charging hydrogen is absorbed and stocked in the metal hydride reactor 2 and the exothermic heat is released to the air side (air temperature is adjusted by the ratio of air from port 31 and ambient). At the same time, the hydrogen already stocked in reactor 1 is released to the fuel cell with a specific mass flow rate, and the required heat for the endothermic desorption is supplied by the liquid desiccant flow. As a result, the temperature of the liquid desiccant can be cooled down to the set point or at least lower than the ambient temperature. These reactors are alternately charged and discharged when operating for a long time and the air and desiccant flow switch accordingly. A power flow diagram is shown in Fig. 3 the small fuel cell provides the power to the battery pack via a DC/DC and at the same time, the battery pack supplies electricity to the motor and compressor via a DC/AC. The small fuel cell in the proposed system acts as a driving range extender. It continuously provides electricity to the motor but will not be affected frequently by the vehicle's driving scenario. This is because the battery is still the power source of the motor which drives the vehicle. Therefore, the H_2 mass flow rate is
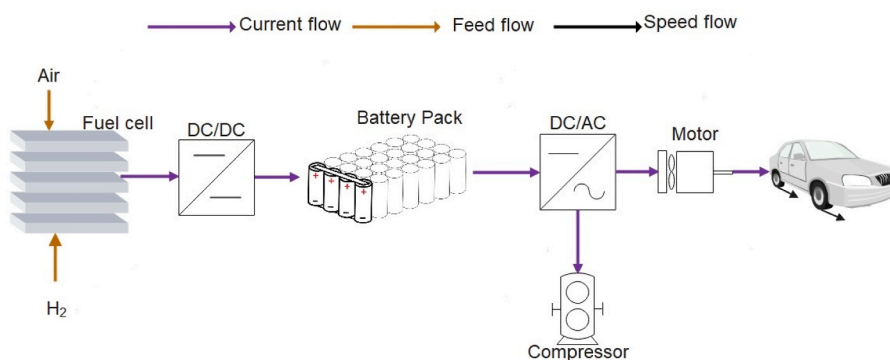
Fig. 3. Schematic diagram of the power flow of the proposed system.
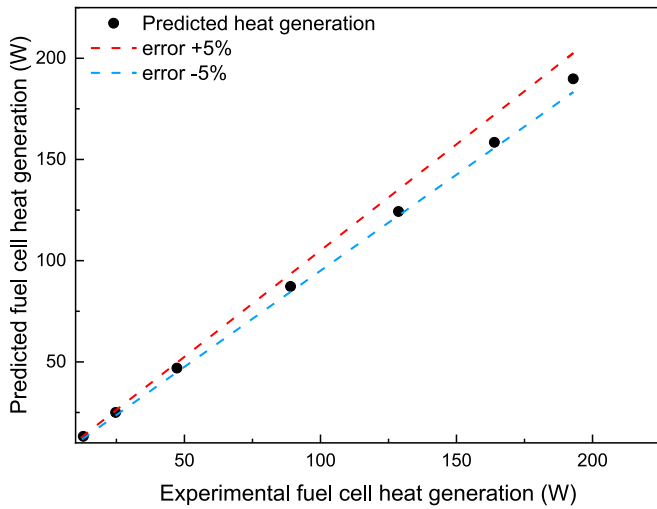
Fig. 4. Fuel cell heat generation model validation.

Fig. 5. Battery thermal model validation.

stable, as a result, the cooling load from the metal hydride can be easily controlled. In case of the cooling capacity provided by the metal hydride is insufficient, the cooling system operating mode can be switched from non-compressive mode to heat pump supplemental mode. Part of the waste heat from the fuel cell can be utilized for the absorption process of the metal hydride, and the remaining waste heat can be used by solution regeneration once the waste heat from the battery pack is not enough due to the driving scenario fluctuations.

3. Model development

3.1. PEMFC and battery model

The heat and power cogeneration characteristic of the Proton-exchange membrane fuel cell (PEMFC) enables simultaneous heat and power supply. Electrochemical and thermodynamic theories are widely adopted to describe the heat generation procedure of the PEMFC. The heat generation of the fuel cell stack is expressed in Eq. (1)

$$Q_{FC} = (V_{nernst} - V_{cell}) \times I_{FC} \tag{1}$$

in which, the V_{nernst} is the Nernst open circuit voltage, V_{cell} is the voltage of a fuel cell, and I_{FC} is the current of the fuel cell. The details of the V_{nernst} can be found in ref. (Albayati et al., 2013).

$$V_{cell} = V_{nernst} + V_{act} + V_{ohm} + V_{con} \tag{2}$$

where V_{act}, V_{ohm}, and V_{con} stands for activation losses, ohmic losses, and concentration losses respectively and details can be found in ref. (Zhang et al., 2023). The H_2 consumption, while operating the fuel cell stack, can be calculated by Eq. (3) (Şefkat and Özel, 2022).

$$\dot{m}_{H_2} = \frac{I_{FC} \times M_{H_2} \times N_{FC}}{2 \times F} \tag{3}$$

in which, M_{H_2} is the molecular weight of the H_2, N_{FC} is the number of fuel cells in the stack and F is Faraday's constant.

For the battery, the heat generation contains parts, namely irreversible heat and reversible heat. The expression is depicted in Eq. (4).

$$Q_{bat} = \underbrace{I_{ch/dch}^2 \times R_{ch/dch}}_{irr} - \underbrace{I_{ch/dch} \times T_{bat} \times \frac{dE_{OC_{bat}}}{dT_{bat}}}_{rev} \tag{4}$$

$I_{ch/dch}$ and $R_{ch/dch}$ represents the battery current and the internal thermal resistance while charging or discharging respectively. $\frac{dE_{OC_{bat}}}{dT_{bat}}$ is the entropy coefficient and T_{bat} is the operating temperature of the battery. The correlations concluded from experimental results can be found in ref. (Mahamud and Park, 2011; Liu et al., 2014). The components parameters and model validation can be found in our previous study (Zhang et al., 2023), in which the predicted results are compared to published results with a deviation of 5%, as shown in Fig. 4. The characteristics of the fuel cell used in this study are shown in Table 1 (see Fig. 5).
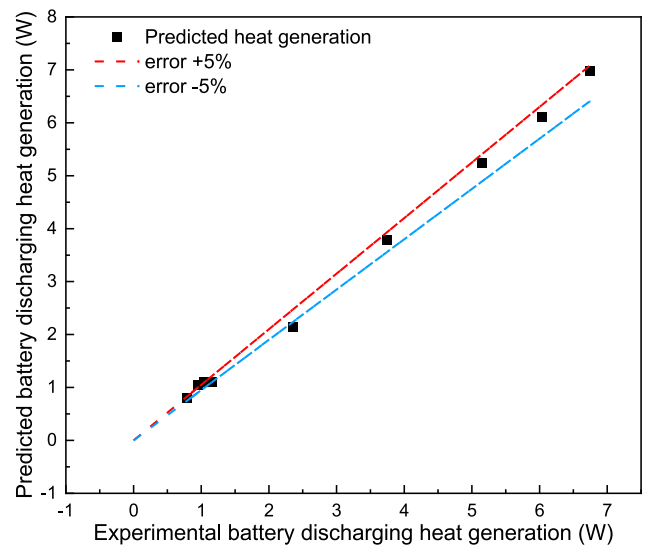
3.2. Open metal hydride thermal model

Metal hydride (MH) is a material that can store hydrogen. In the open metal hydride system, the absorption and desorption processes are driven by the pressure difference between the inlet and the outlet. The reversible reaction can be described as follows, which is an exothermic reaction.

$$Me(s) + \frac{X}{2} \times H_2(g) \rightleftharpoons MH_X(S) + \Delta H \tag{5}$$

and the maximum cooling capacity during desorption is shown in Eq. (6),

$$Q_{MH,des,max} = \dot{m}_{H_2} / M_{H_2} \times \Delta H_{des} \tag{6}$$

where ΔH_{des} (J/mol) is the heat of formation. The temperature change of the MH can be calculated below:

$$[(1-\varepsilon) \times \rho_{MH} \times Cp_{MH} + \varepsilon_{MH} \times \rho_{H2} \times Cp_{H2}] \times \frac{\partial T_{MH}}{\partial t} + \nabla(-\lambda_{eff} \times \nabla T) = Q_{MH} \tag{7}$$

Table 1
Characteristics of the fuel cell.

Parameters	Value	Unit
Fuel cell (Robaina and Neves, 2021; Crabtree, 2019)		
Operating temperature (T_{FC})	65	°C
Inlet O2 pressure ($P_{O2,in}$)	2.5	atm
Inlet H2 pressure ($P_{H2,in}$)	2.4	atm
Number of cells	40	/
Area of cell (A_{FC})	285.8	cm^2
Thickness of cell (l_{FC})	5.1X10-3	cm^3
Efficiency	50	%
Membrane wetting level	23	/
Limited current density (i_{max})	2.2	A/cm2
Rated power	8.698	kW

in which ε_{MH} is the porosity of the MH which is 0.67 (Weckerle et al., 2017), ρ_{MH} and Cp_{MH} are the density and specific heat capacity of the solid MH and ρ_{H2} and Cp_{H2} are the density and specific heat capacity of the hydrogen. λ_{eff} is the effective heat conductivity of the MH bed. In order to utilise the cooling capacity, a separating steel plate and the heat transfer fluid, which is the liquid desiccant solution in the proposed system, is needed. Based on (Weckerle et al., 2019b), the energy balance for the designed separating plate is considered as Eq. (8).

$$\rho_{SP}Cp_{SP}bd_{SP}l\frac{\partial T_{SP}}{\partial t} + \nabla\Big(-\lambda_{SP}bd_{SP}l\nabla T_{SP}\Big) = bl\Big[\big[h_{MH}(T_{MH} - T_{SP}) - h_{sol}(T_{SP} - T_{sol})\big] \tag{8}$$

where b and l are the width and length of the reactor, d_{SP} is the thickness of the separating plate. h_{MH} and h_{sol} are the convective heat transfer coefficient of the MH and liquid desiccant solution. The h_{sol} is given by:

$$\frac{h_{sol} \times \lambda_{sol}}{d_{h,sol}} = 0.205 \times Pr_{sol}^{\frac{1}{3}} \times \big[f_{ges} \times Re_{sol}^2 \times sin\,(2\beta)\big]^{0.374} \times \frac{\mu_{sol}}{\mu_{sol,wall}} \tag{9}$$

where μ_{sol} and $\mu_{sol,wall}$ are the dynamic viscosity of the solution in the middle of the channel and at the wall. β is the inclination angle of a chevron pattern plate heat exchanger. f_{ges} is called the fanning friction factor which can be expressed as:

$$f_{ges} = \left\{\frac{cos\,(\beta)}{\big[0.045 \times tan(\beta) + 0.09 \times sin(\beta) + \frac{16}{Re_{sol}} \times cos\,(\beta)^{-1}\big]^{0.5}} + \frac{1 - cos\,(\beta)}{\left(\frac{37.05}{Re_{sol}^{0.0289}}\right)^{0.5}}\right\}^{0.5} \tag{10}$$

The Prandtl number and Reynolds number are defined by

$$Pr_{sol} = \frac{\mu_{sol} \times \rho_{sol} \times Cp_{sol}}{\lambda_{sol}} \tag{11}$$

$$Re_{sol} = \frac{v_{sol} \times d_{h,sol}}{\mu_{sol}} \tag{12}$$

where v_{sol} is the velocity of the solution inside the channel and $d_{h,sol}$ is the hydraulic diameter of the solution flow channel. For the solution temperature, the energy balance equation along the solution flow direction x is defined as:

$$\rho_{sol} \times Cp_{sol} \times b \times l \times d_{sol} \times \frac{\partial T_{sol}}{\partial t} + \dot{m} \times Cp_{sol} \times l \times \frac{\partial T_{sol}}{\partial x} = h_{sol} \times b \times l \times (T_{SP} - T_{sol}) \tag{13}$$

The specifications of the metal hydride are displayed in Table 2.

The thermal model of the proposed metal hydride reactor during the desorption process is validated depending on the outlet temperature of the heat transfer fluid in the ref. (Weckerle et al., 2019b). The desorption process of the open metal system is similar to the solid green line shown in Fig. 2. In order to examine the model, the property of the heat transfer fluid, initial metal hydride temperature, and the dimensions of the rector are defined as variable parameters in this work. The outlet temperature of the heat transfer fluid is used to validate the proposed thermal model of the metal hydride reactor in this study. The results are shown in Fig. 6 and the deviation is always within 5%. Also, the characteristic of the metal hydride's pressure variation along with its hydrogen capacity is validated by comparing it to the results in ref (Weckerle et al., 2019b). and the changes in metal hydride's pressure, when the fuel cell current output is 5 kW, are shown in Fig. 7. During the process, the metal hydride 1 desorbs for 150s till the pressure reached 9 bar and then metal hydride 2 started desorbing for another 150s (see Fig. 8).

Table 2
Specifications of the metal hydride.

Parameters	Value	Units
MH Specifications (COP 26 in Glasgow, 2021)		
Material	Hydralloy C2	/
Mass per metal hydride (m_{MH})	1.55	kg
Density (ρ_{SP})	6375.3	Kg/m^3
Heat conductivity (λ_{eff})	1	W/(m·K)
Heat transfer coefficient	1×10^4	W/(m^2·K)
Maximum hydrogen capacity (W_{max})	1.7	%
Lowest hydrogen capacity (W_{min})	0.47	%
Porosity (ε)	0.67	
Specific heat capacity (Cp_{MH})	500	J/(kg·K)
Operating Conditions		
Regeneration temperature ($T_{MH,reg}$)	35	°C
Discharging temperature ($T_{MH,dch}$)	30	°C
Maximum pressure	30	bar
Lowest pressure	9	bar
Maximum hydrogen capacity (W_{max})	1.7	%
Lowest hydrogen capacity (W_{min})	1.3	%
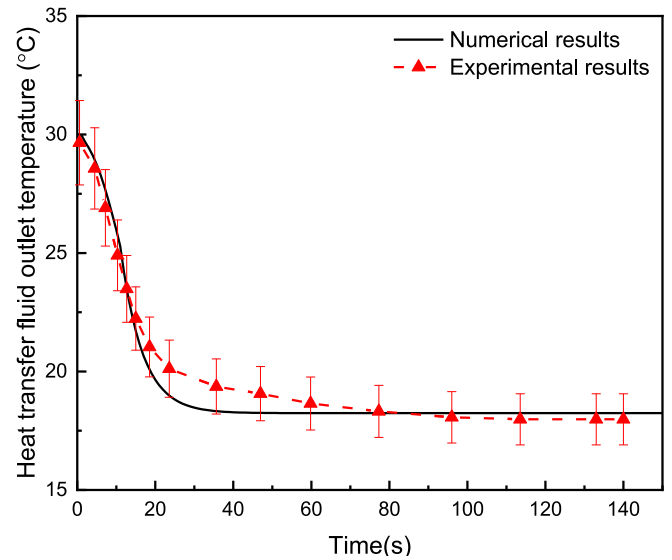
Fig. 6. Open metal hydride thermal model validation compared to ref (Weckerle et al., 2019b).
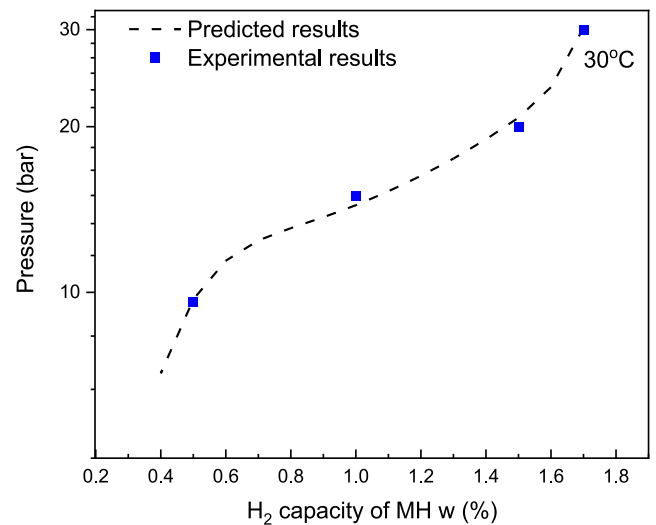
Fig. 7. Metal hydride's pressure variation along with its hydrogen capacity.
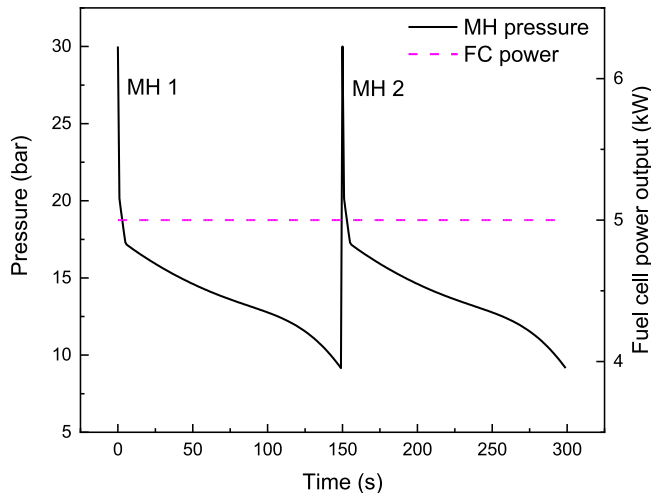
Fig. 8. Characteristic curve of the pressure of the metal hydride.

3.3. Hollow fibre liquid desiccant dehumidifier heat and mass transfer model

A one-dimensional model for air and liquid desiccant solution flow was developed in this study due to the homogenous transverse variables (Zhang et al., 2019a).

$$\frac{\dot{m}_{sol}}{n_{eq}d_i} \times \frac{\partial T_{sol}}{\partial y} \times Cp_{sol} = U_{de,h} \times (T_{air} - T_{sol}) + i_{fg} \times K_{de,m} \times \rho_{air} \times (\omega_{air} - \omega_{sol}) \tag{14}$$

$$\frac{\dot{m}_{sol}}{n_{eq}d_i} \times \frac{\partial X_{sol}}{\partial y} = K_{de,m} \times \rho_{air} \times (\omega_{air} - \omega_{sol}) \tag{15}$$

$$\frac{\dot{m}_{air}}{n_{ach}d_h} \times Cp_{sol} \times \frac{\partial T_{air}}{\partial x} = U_{de,h} \times (T_{sol} - T_{air}) \tag{16}$$

$$\frac{\dot{m}_{air}}{n_{ach}d_h} \times \frac{\partial \omega_{air}}{\partial x} = K \times (\omega_{sol} - \omega_{air}) \tag{17}$$

In Eq. (14) to (17), x is the direction of the solution flow along the hollow fibres while y is the direction of the cross-air flow. n_{eq} and n_{ach} are the equivalent number of fibres and airflow channel numbers respectively. d_i and d_h represent the inner diameter of hollow fibres and the hydraulic diameter of the airflow channel respectively. $U_{de,h}$ (W/m^{2}K) is the overall heat transfer coefficient while $K_{de,m}$ (m/s) is the overall mass transfer coefficient. X_{sol} is the concentration of the solution and ω (kg/kg) is the specific humidity. The expressions of the specific humidity and concentration of the solution are shown below (Fumo and Goswami, 2002).

$$\omega_{sol} = 0.622 \times \frac{P_{sol}(X_{sol}, T_{sol})}{P_{atm} - P_{sol}(X_{sol}, T_{sol})} \tag{18}$$

in which, P_{sol} is the vapour pressure of the solution at a particular concentration and temperature. The concentration of the solution is also a function of temperature which can be obtained in Ref. (Melinder, 2007). The expressions of the $U_{de,h}$ and $U_{de,m}$ is defined as the following equations.

$$\frac{1}{U_{de,h}} = \left[\frac{1}{h_{de,sol}} \times \left(\frac{d_o}{d_i} \right) + \frac{\delta}{\lambda_m} \times \left(\frac{d_o}{\overline{d}} \right) + \frac{1}{h_{de,air}} \right] \tag{19}$$

$$\frac{1}{K_{de,m}} = \left[\frac{1}{k_{de,sol}} \times \left(\frac{d_o}{d_i} \right) + \frac{\delta}{D_m} \times \left(\frac{d_o}{\overline{d}} \right) + \frac{1}{k_{de,air}} \right] \tag{20}$$

where, δ is the thickness of the membrane, D_m (m/s) is the mass diffu-

sivity of the hollow fibre, and λ_m (W/mK) is the thermal conductivity of the hollow fibre. The heat transfer coefficients for solution and air are calculated based on the following equations (Pakowski, 2007; Zhang et al., 2000):

$$\frac{h_{de,sol} \times d_h}{\lambda_{sol}} = 3.658 + \frac{0.085 \times \left(\frac{Re_{sol} \times Pr_{sol} \times d_h}{L} \right)}{1 + 0.047 \times \left(\frac{Re_{sol} \times Pr_{sol} \times d_h}{L} \right)^{0.67}} \times \left(\frac{\mu_{sol}}{\mu_w} \right)^{0.14} \tag{21}$$

$$\frac{h_{de,air} \times d_h}{\lambda_{air}} = 1.33 \times 0.648 \times Re_{air}^{0.198} \times Pr_{air}^{\frac{1}{3}} \tag{22}$$

And the mass transfer coefficient for the solution side and air side can be calculated based on Eq. (23) to (24) respectively (Zhang, 2011).

$$\frac{k_{de,sol} \times d_h}{D_{w,sol}} = 1.62 \times \left(\frac{d_i^2 \times u_{sol}^2}{L \times D_{w,sol}} \right)^{\frac{1}{3}} \tag{23}$$

$$\frac{k_{de,air} \times d_h}{D_{w,air}} = \left(14.06\varphi^4 - 29.21\varphi^3 + 22.59\varphi^2 - 7.71\varphi \right.$$
$$\left. + 1.03 \right) Re_{air}^{0.33} \left(\frac{\mu_{air}}{\rho_{air} D_{w,air}} \right)^{0.33} \left(0.882 D_f - 0.535 \right) \tag{24}$$

Where φ is the packing fraction of the dehumidifier, $D_{w,air}$ and $D_{w,sol}$ stand for water diffusivity in air and solution respectively. D_f is the fractal dimension of the fibre packing, the value of that can be found in Ref. (Zhang, 2006). The hollow fibre liquid desiccant dehumidifier model is validated in our previously published study (Zhang et al., 2019a) and the results are shown in Fig. 9.

3.4. Heat pump model

There are five main components in this study's proposed heat pump cycle. Two evaporators (called chiller and evaporator), a compressor, a plate condenser, and an expansion valve. The heat transfer model for the plate-type evaporator, compressor and expansion valve has been developed and validated in our previously published work from a component perspective (Zhang et al., 2023). The heat transfer model for the adopted plate-type condenser is developed in this sub-chapter. The heat transfer process in the condenser includes three regions: vapour de-superheating region, two-phase region, and liquid subcooling region. In this study, the vapour de-superheating region and the two-phase region are considered together as the heat transfer rate only accounts for a small fraction (1.4%–1.6%) (Zhang et al., 2019b). For the two-phase region, the heat transfer coefficient for the refrigerant side is
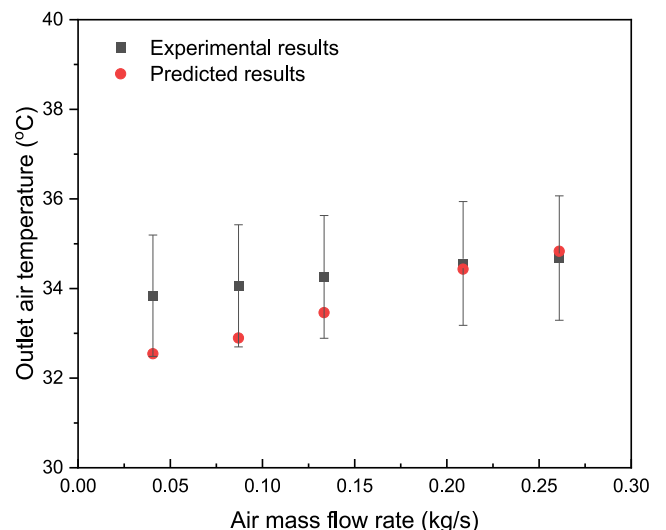
Fig. 9. Validation of the dehumidifier.

considered as (Yan et al., 1999):

$$h_{cond,ref} = \frac{4.118 \times Re_{eq}^{0.4} \times Pr_{cond,ref}^{\frac{1}{3}} \times \lambda_{cond,ref}}{D_h} \qquad (25)$$

in which, the Re_{eq} is the equivalent Reynolds number which is defined as:

$$Re_{eq} = \frac{\dot{m}_{ref} \times \left[1 - X_m + X_m \times \left(\frac{\rho_{ref,lq}}{\rho_{ref,vp}}\right)^{0.5}\right] \times D_h}{A_{cross} \times \mu_{ref,lq}} \qquad (26)$$

where $\dot{m}_{ref}$ is the refrigerant mass flow rate, A_{cross} is the flow channel cross-section area. X_m is the average vapour quality between the inlet and outlet of the two-phase region and $\rho_{ref,lq}$ and $\rho_{ref,vp}$ are the density of the liquid and vapour refrigerant respectively. For the single-phase liquid desiccant solution, the single-phase correlation for water was adopted (Zhang et al., 2019b).

$$\frac{h_{cond}d_h}{\lambda_{cond}} = 0.4225 Re_{cond}^{0.733} Pr_{cond}^{1/3} \left(\frac{\mu_{cond}}{\mu_{wall}}\right)^{0.14} \qquad (27)$$

For the liquid subcooling region, Eq. (27) is utilized for both the refrigerant side and the solution side. Therefore, the overall heat transfer coefficients for these two regions are depicted below:

$$\frac{1}{U_{cond}} = \frac{1}{h_{cond,ref}} + \frac{\sigma_{wall}}{\lambda_{wall}} + \frac{1}{h_{cond}} \qquad (28)$$

The conservation of energy of the condenser can be described as:

$$\dot{Q}_{cond} = U_{cond} \times A_{cond} \times LMTD_{cond} \qquad (29)$$

$$\dot{Q}_{cond,ref} = \dot{m}_{ref} \times Cp_{ref} \times \Delta T_{cond,ref} \qquad (30)$$

$$\dot{Q}_{cond,des} = \dot{m}_{cond,des} \times Cp_{des} \times \Delta T_{cond,des} \qquad (31)$$

The condenser model and evaporator model were validated with the published results in ref (Yan et al., 1999). and (Yan and Lin, 1999) as shown in Fig. 10.

For the compressor model, the correlation introduced by Ref (Tian et al., 2018). was adopted. The compressing ratio (γ) and the compressor power consumption are important. Kinab et al. (2010) concluded the relationship between refrigerant temperature and mass flow rate for a fixed compressor speed:

$$\dot{m}_{ref} = b_0 + b_1 t_{eva} + b_2 t_{eva}^2 + b_3 t_{eva}^3 + b_4 t_{cond} + b_5 t_{cond}^2 + b_6 t_{cond}^3 + b_7 t_{eva} t_{cond}$$
$$+ b_8 t_{eva}^2 t_{cond} + b_9 t_{eva} t_{cond}^2 \qquad (32)$$

in which coefficients b_0 to b_9 can be obtained from Ref. (Tian et al., 2018). The power consumption of the compressor is shown below:

$$W_{comp} = \frac{\dot{m}_{ref} \times (H_{dis} - H_{suc})}{\eta_{isen}} \qquad (33)$$

in which H_{dis} and H_{suc} are the enthalpy of R134a at the suction and exit of the compressor respectively, η_{isen} is the isentropic effectiveness of the compressor which is assumed to be 0.67 (Cuevas et al., 2012). The EEV throttle process is considered an isenthalpic process and the mass flow rate flow through the EEV can be calculated as below:

$$\dot{m}_{EEV} = C_v \times A_c \sqrt{2 \times \Delta P_{EEV} \times \rho_{ref\_in}} \qquad (34)$$

where A_c is the circulation area while C_v is the flow coefficient, and $C_v = 0.02005 \times \sqrt{\rho_{in}} + 0.634/\rho_{out}$ (Tian et al., 2020). The validation of the compressor model is shown in Fig. 11 and a conclusion of the maximum error margin of each component is illustrated in Fig. 12.

3.5. Performance indicator

In order to evaluate the efficiency of the system, the Coefficient of Performance (COP) is introduced in this study. The COP in this study is defined as below:

$$COP = \frac{Q_{cool}}{W_{hp}} \qquad (35)$$

in which Q_{cool} is the cooling capacity provided by the liquid desiccant
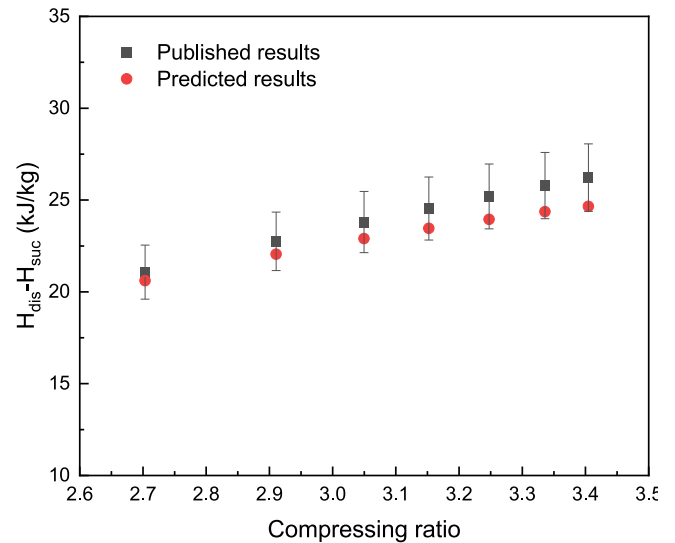
Fig. 11. Validation of the compressor (Guo et al., 2011).
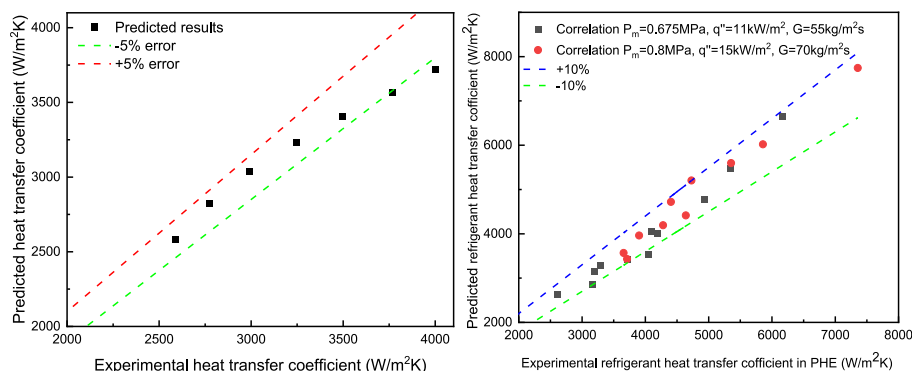
Fig. 10. Condenser (left) and evaporator (right) model validation by comparing to the experimental data.
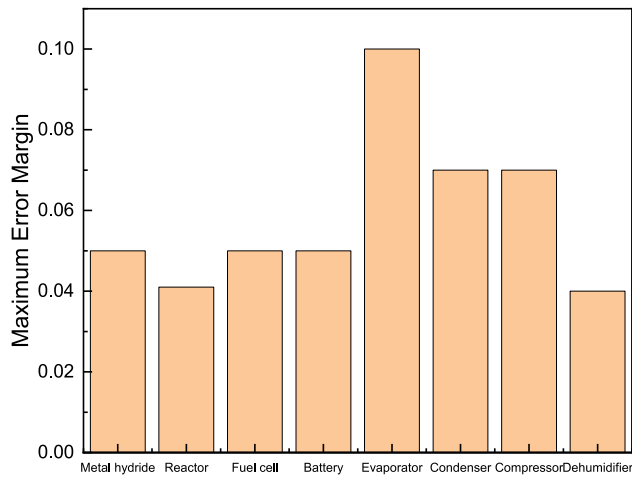
Fig. 12. Component level maximum error margin conclusion.

dehumidifier, the expression of which is defined in Eq. (36) W_{hp} is the heat pump energy consumption when it is required.

$$Q_{cool} = m_{air} \times \left(H_{air,in} - H_{air,out} \right) \tag{36}$$

where, $H_{air,in}$ and $H_{air,out}$ are the enthalpy of the inlet air and outlet air of the dehumidifier respectively.

The specifications of the components in the proposed system are shown in Table 3.

3.6. Simulation procedure

The numerical model for the proposed system is programmed in MATLAB. The physical characteristics of the refrigerant R134a were sourced from the embedded REFPROP in MATLAB. The model includes a fuel cell and battery model, a heat pump model, an open metal hydride system model, and a liquid desiccant solution (KCOOH) dehumidification and regeneration model. Those models were integrated with the following assumptions and the flow chart of the simulation process is shown in Fig. 13. The simulation started from the chiller side in order to make sure that all the waste heat generated by the battery pack could be released to keep the battery pack can always operating under an optimal temperature. Several input assumptions were made, and these assumptions were required to be adjusted based on the energy conservation (error<0.0001) in the chiller, evaporator, dehumidifier, and condenser respectively. In the end, outputs such as air temperature, relative humidity, and COP could be achieved. The operating conditions and working flow constant physical properties are shown in Table 4.

(1) The temperature of the outlet coolant was set at 25 °C and the temperature difference of the battery coolant at the inlet and outlet of the chiller was controlled at 4 °C in order to maintain the temperature consistency of the battery pack (Akbarzadeh et al., 2021).

(2) The thermophysical properties of the liquid desiccant KCOOH and metal hydride bed, such as density, heat conductivity, etc., are assumed to be constant.

(3) In the dehumidifier, the water molecules' diffusion and heat conduction along the solution flow direction was ignored (Seyed-Ahmadi et al., 2009).

(4) The pressure drop in the heat exchanger was neglected and the de-superheating region was combined into the two-phase region (Zhang et al., 2019b).

Table 3
Specifications of the components.

Components	Type	Specifications
Compressor	Scroll	Displacement: 27 cm^3/s Nominal power: 2.5 kW Speed: 2000 RPM
Chiller	Plate type	Number of plates: 30 Plate size: 60 × 160 mm^2 Channel space: 2.0 mm
Evaporator	Plate type	Number of plates: 30 Plate size: 60 × 160 mm^2 Channel space: 2.0 mm
Condenser	Plate type	Number of plates: 30 Plate size: 60 × 160 mm^2 Channel space: 2.0 mm
Dehumidifier	Hollow fibre type	Module cross section: 0.2 m Module height: 0.7 m Number of fibres: 6500 Fibre outer diameter: 1.6 mm Fibre inner diameter: 1.4 mm Porosity: 0.6 Packing fraction: 0.32
Metal hydride reactor	Plate type	Number of separating plates: 36 Plate size: 0.279 × 0.08509 m^2 Channel space: 8.8 × 10^{-4} m Porosity: 0.67 Thickness of separating plates: 4 × 10^{-4} m
Fuel cell	PEMFC	Number of cells: 40 Thickness of fuel cell: 5.1 × 10^{-3} cm Area of cell: 285.8 cm^2
Battery pack	Modified based on Tesla Model S (TRANSPORTATION USDO, 2013)	Pack capacity: 60kWh Number of batteries: 1764 Number of batteries in series for one module: 6 Number of batteries in parallel for one module: 21 Number of modules: 14 Battery capacity: 8Ah Battery voltage: 4.2V

(5) The temperature variation along the direction perpendicular to the flow of solution and the heat losses in the metal hydride reactor were ignored (Weckerle et al., 2019b).

(6) The inlet solution temperature of the open metal hydride system was assumed to be very close to the ambient temperature after being cooled by the ambient air.

(7) The desorption duration of a metal hydride is assumed 150s when the switching criterion (P$_{MH,out}$<9 bar) is reached.

(8) The pressure inside the metal hydride is assumed to drop to 20 bar immediately due to the free volume expansion that occurs during the beginning of the transition between two metal hydrides (Weckerle et al., 2019a).

4. Results and discussions

4.1. Performance of the non-compressive cooling and dehumidification cycle

4.1.1. Impacts of the ambient temperature

In the non-compressive cooling cycle, the compressor is not utilized in the cooling system and the cooling capacity is provided by the open metal hydride system. Fig. 14 shows the influence of the ambient temperature on the performance of the non-compressive cooling system.
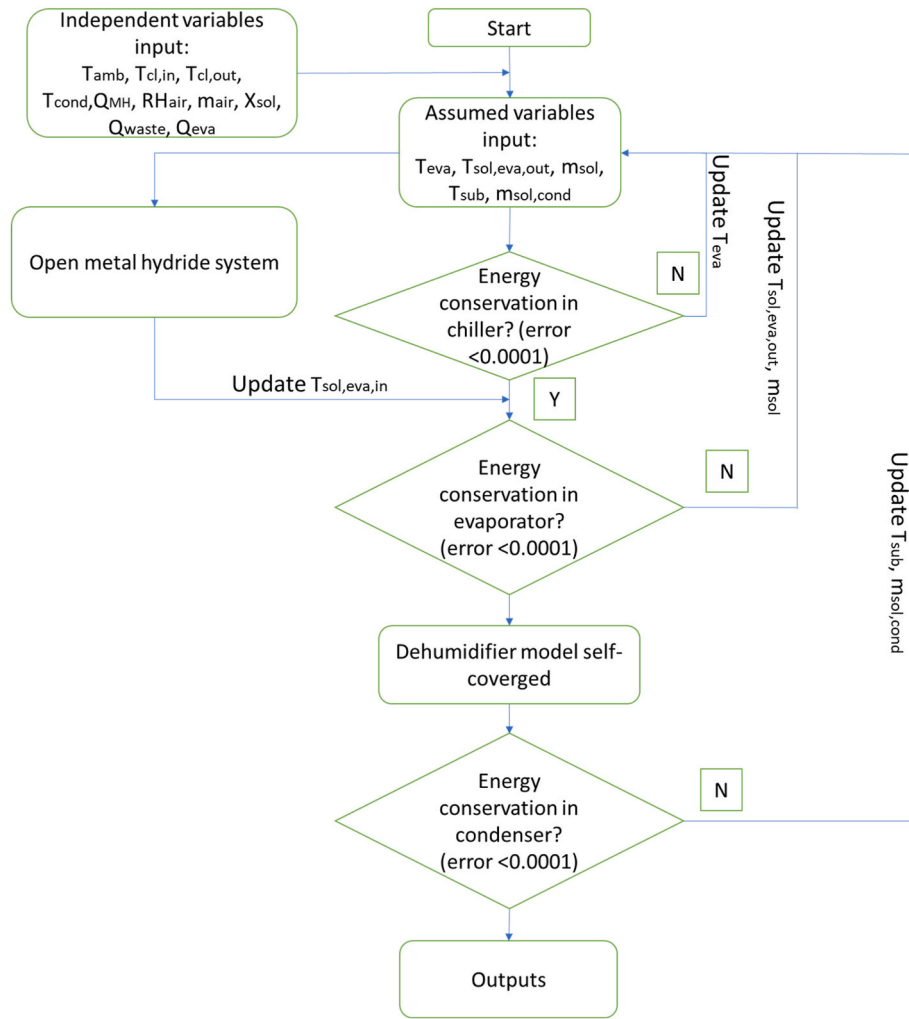
Fig. 13. Numerical model simulation flow chart.

Table 4
Operating conditions and demanded load profile in the simulation.

Parameters	Value	Unit
Fuel cell temeprature	65	°C
Battery temperature	25	°C
Ambient temperature (T_{amb})	26-30 (std:30)	°C
Ambient relative humidity (RH_{air})	80	%
MH max pressure	30	bar
MH lowest pressure	9	bar
MH absorbtion temperature ($T_{MH,abs}$)	35	°C
MH desorption temperature ($T_{MH,des}$)	30	°C
Battery discharging C rate (B_{dch})	0.45–0.66 (std:0.5755)	C
Battery charging C rate (B_{ch})	0.05–0.18 (std: 0.1364)	C
Solution working temperature ($T_{sol,eva,o}$)	15–23	°C
Solution working concentration ($X_{sol,eva,o}$)	62	%
Air mass flow rate	0.07	kg/s
Cooling demands	2–4	kW
Cabin temperature set point	25	°C
Cabin relative humidity set point	50	%

With the increasing ambient air temperature, the air outlet temperature, specific humidity, and the proposed system's cooling capacity increase. As shown in Fig. 14(a) and (b) when the ambient temperature increases from 26 °C to 34 °C with an unchangeable air mass flow rate of 0.03 kg/s and 1 kW of QMH, the air outlet temperature increases from 23.25 °C to 25.69 °C, and the specific humidity also increased by 38%. This is because raising the ambient temperature also leads to a raising of the

air-specific humidity when the RH is constant. Both of them cause more heat and mass transfer between the solution and air in the dehumidifier. However, the sensible heat and latent heat during mass dehumidification will increase the temperature of the solution dramatically and as a result, increase the water vapour partial pressure of the solution which reduces the ability to transfer mass and possibly transfer heat back to the air according to Eq. (14)–(17). This is perhaps the reason why the temperature-increasing gradient increases significantly with the increase in the ambient air temperature. Although the decrease in both air temperature and air specific humidity, compared to the inlet conditions, because of the increase of the ambient air temperature, the cooling capacity still increases. This is because the increasing rate in air outlet temperature and air specific humidity is always lower than that in ambient temperatures. For example, when the ambient air temperature and specific humidity increase by 30.5% and 60%, the outlet air temperature and specific humidity only increase by 28% and 52.6% respectively in the worst-case scenario (m_{air} = 0.07 kg/s). Furthermore, when the air mass flow rate increases from 0.03 kg/s to 0.05 kg/s to0.07 kg/s, the air outlet temperature, specific humidity, and cooling capacity also increase. This is due to the increasing heat and mass transfer rate in terms of Eq. (21)–(24) and less time consumed by a unit volume of solution flowing through a dehumidifier. But the impacts of the air mass flow rate on air temperature, specific humidity, and cooling capacity decrease with the increase of the mass flow rate because of the capacity limit of the polymer hollow fibre heat and mass exchanger. So, when the ambient temperature increases, the air mass flow rate should be adjusted
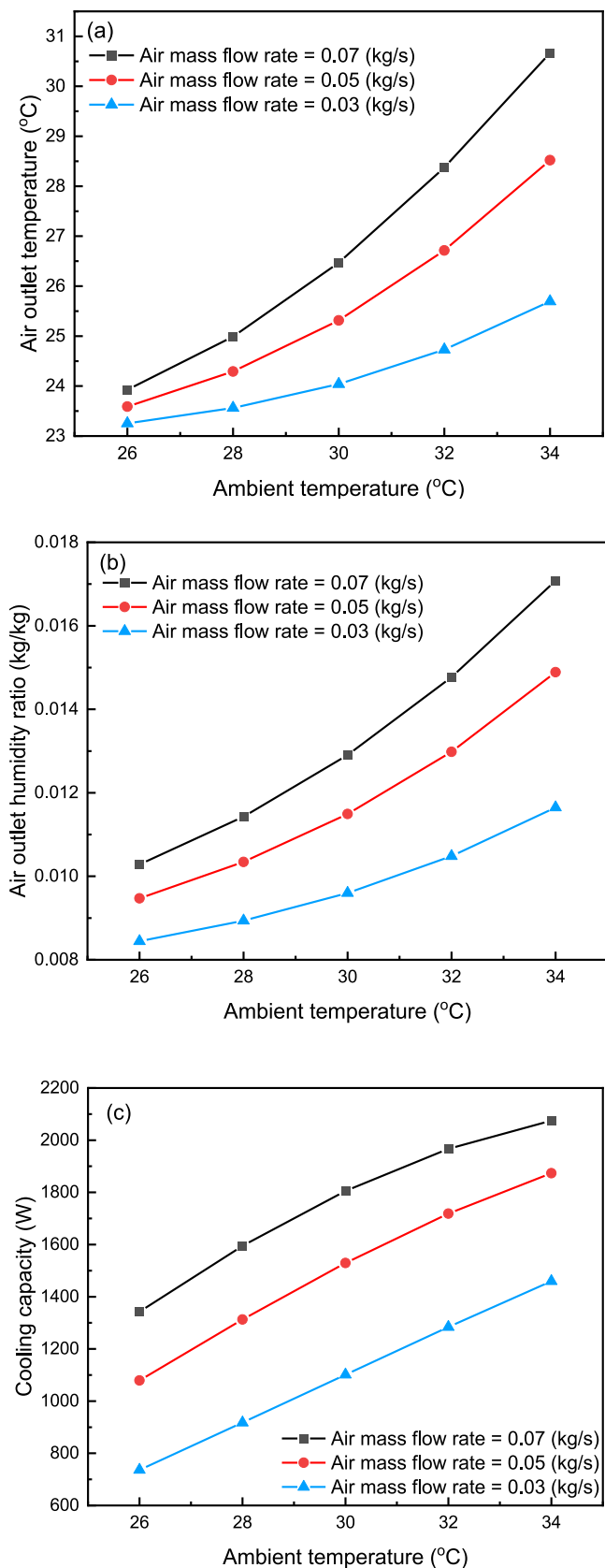
Fig. 14. The impacts of the ambient temperature and air mass flow rate on air outlet temperature (a), specific humidity (b), cooling capacity (c) (RH_{air} = 80%, X_{sol} = 62%, B_{ch} = 0.1, $T_{sol,MH,out}$ = 23 °C).

in order to provide sufficient inlet air if other parameters are not changed.

4.1.2. Impacts of battery charging C rate

The impact of the battery charging C rate on ambient air temperature and air specific humidity is opposite to that of the ambient temperature. The battery charging current is supplied by the fuel cell stack and the H_2 required by the fuel cell stack is provided by the vessel via an open metal-hydride cooling system. Therefore, the increasing battery discharging C rate also represents an increase in the mass flow rate flow through the MH and the cooling capacity of the adopted open-metal hydride system. As a result, due to the stable inlet and outlet solution temperature of the open-metal hydride system, the solution mass flow rate across the MH and evaporator increases correspondingly. Based on the variation in solution mass flow rate, the average temperature, and water vapour partial pressure of the solution in the dehumidifier decline. Hence, the temperature and equivalent specific humidity differences between the air and solution in Eq. (14)–(17) increase and cause greater variations in air temperature and specific humidity and lead to a decrease in air outlet temperature and outlet air specific humidity. The results in Fig. 15(a) and (b) reflect the analysis above. For instance, when air mass flow is 0.05 kg/s, the battery charging C rate increases from 0.05 to 0.18, the air outlet temperature decreases from 28 °C to 23.8 °C and the air outlet specific humidity drops from 0.013 kg/kg to 0.0105 kg/kg. Furthermore, the decrease in air mass flow rate will weaken the impacts of the battery discharging C rate. For example, when the battery discharging C rate increases from 0.05 to 0.1, the outlet air temperature decreases by 4%, 9.6%, and 10.8% for air mass flow rate of 0.03 kg/s, 0.05 kg/s, and 0.07 kg/s respectively. This is due to the lower heat and mass transfer coefficient and lower driving force caused by the deeper cooled and dehumidified air inside the dehumidifier. The battery charging C rate has a similar impact on cooling capacity compared to ambient temperature. As shown in Fig. 15, the cooling capacity increases by 46% when the air mass flow rate equals 0.05 kg/s and the battery charging C rate increases by 2.34 times. However, the principle behind the influence is different. For the battery charging C rate, it increases the heat and mass transfer by increasing the solution mass flow rate which allows more heat and moisture to be absorbed by the solution.

4.1.3. Impacts of liquid desiccant solution working temperature

The solution working temperature is also an important parameter for the performance. As shown in Fig. 16(a), with the decreasing solution working temperature, from 23 °C to 15 °C, the air outlet temperature also decreases from 23 °C to 18.5 °C when the air mass flow rate is 0.03 kg/s. This is because of the increasing temperature difference between the solution side and the air side, according to Eq. (16). But when the air mass flow rate increases to 0.05 kg/s and 0.07 kg/s, the decreasing speed drops, and a similar trend can be observed when the solution temperature is lower. For example, the reductions in the air outlet temperature are only 9.5% and 5.4% for the air mass flow rate of 0.05 kg/s and 0.07 kg/s respectively. Also, when the air mass flow rate is 0.05 kg/s, with the solution working temperature decreasing from 23 °C to 21 °C, the outlet air temperature decreases by 4%. However, when the solution working temperature decreases from 19 °C to 17 °C, the outlet air temperature only decreases by 3%. The main reason is the increasing latent heat caused by the increasing absorbed water vapour makes the solution temperature higher than the air and starts transferring heat to the air side. The increasing absorbed water vapour can be found in Fig. 16(b). When the air mass flow rate is 0.03 kg/s, the outlet air specific humidity decreased by 14.5% when the solution working temperature descends from 23 °C to 15 °C. However, it should be noted that when the air mass flow rate increased to 0.07 kg/s, the change in air outlet specific humidity can be ignored. This is because the decreasing solution working temperature also reduces the solution mass flow rate. Although at lower solution working temperature, the initial greater temperature difference
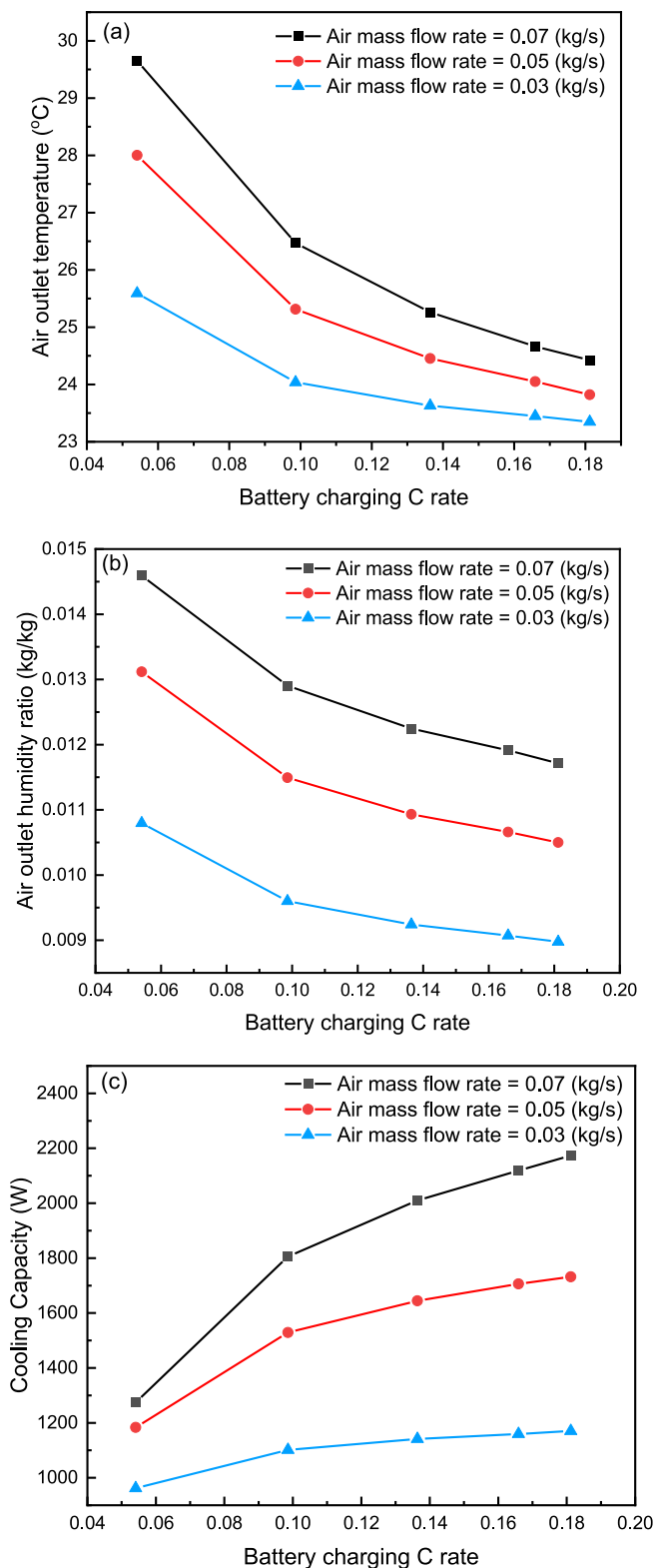
Fig. 15. The impacts of the battery charging C rate and air mass flow rate on air outlet temperature (a), specific humidity (b), cooling capacity (c) (RH$_{air}$ = 80%, X$_{sol}$ = 62%, T$_{amb}$ = 30 °C, T$_{sol,MH,out}$ = 23 °C).

Fig. 16. The impacts of the solution temperature and air mass flow rate on air outlet temperature (a), specific humidity (b), cooling capacity (c) (RH$_{air}$ = 80%, X$_{sol}$ = 62%, T$_{amb}$ = 30 °C, B$_{ch}$ = 0.1).

between the inlet air and inlet solution will increase the heat transfer rate, the temperature increase in the solution is also substantial due to the lower solution mass flow rate, causing the water vapour partial pressure in a solution to easily achieve the same level as that in the air. The impacts of the solution working temperature on cooling capacity

show a reverse trend compared to that on outlet air temperature and specific humidity. As depicted in Fig. 16(c), the cooling capacity increases with the decreasing solution working temperature. For example, the cooling capacity increased by 276W when the solution working temperature was reduced from 23 °C to 15 °C. This is the outcome of the decreasing outlet air specific humidity and temperature However; the impact is also not obvious when the air mass flow rate is 0.07 kg/s.

4.1.4. Real time performance

In order to provide continuous cooling capacity to the cabin, two MHs should be used alternately. However, since the absorption temperature is higher than the desorption temperature, the system cannot always provide maximum and stable heat to the solution due to the heat loss that occurs when switching operation modes between the two MHs. Once the transition occurs, the effects of fluid exchange losses and heat losses can be observed. As shown in Fig. 17, there is an 800W loss at the beginning of the transition and it will take approximately 46s to reach the stable stage. In the recovery stage, due to the heat loss, the solution temperature will increase which leads to an increase in outlet air dry bulb temperature. The outlet air dry bulb temperature peaked at 7s and dropped to the ambient level at 12s. However, the proposed system not only cools the air temperature but also dehumidifies the supply of air. The duration of time that the outlet air wet-bulb temperature is higher than the inlet air wet-bulb temperature is shorter than the time that the outlet air dry-bulb temperature is higher than the temperature of the inlet air. The duration is only 5s, which occurs between 4s and 9s, greatly reducing the duration of discomfort when the heat pump is not involved. In the stable stage, the proposed non-compressive cooling and dehumidification system can always provide the supply air with a wet bulb temperature of 17.8 °C which equals the wet bulb temperature under 25 °C and 50% RH.

In order to provide continuous cooling capacity to the cabin, two MHs should be used alternately. Therefore, the proposed open-metal hydride-assisted non-compressive cooling and dehumidification system can successfully cool down the supply air to the set point, which is 25 °C with 50%RH. However, the cooling performance of the proposed system is affected by several factors such as the ambient temperature, air mass flow rate, battery charging C rate, and solution working temperature. For a certain battery charging C rate that corresponds to the fuel cell output, there is a limit to the outlet air mass flow rate. Exceeding the limit, the system cannot provide sufficient supply air, although the cooling capacity may meet the requirements. Meanwhile, higher ambient air temperature and RH also bring negative effects on performance. Increasing the fuel cell power output may be a solution, but it

strongly depends on the State of Charge (SOC) of the battery and the fuel cell's maximum current density limitation. When conditions permit, the proposed system can provide enough cooling capacity with sufficient air temperature and RH to the cabin without extra power consumption. However, since the absorption temperature is higher than the desorption temperature, the system cannot provide stable cooling loads during the transitions. Moreover, in practice, the battery charging C rate cannot be infinitely high to provide for high cooling demands scenarios such as start-up stage or high ventilation requirement and the fluctuations during MHs' transition needed to be avoided. As a result, a heat pump system could be adopted as a supplement to the proposed cooling and dehumidification system to overcome severe operating situations and utilise more waste heat for solution regeneration.

4.2. Performance of the metal hydride assisted cooling and dehumidification cycle with supplement of heat pump

4.2.1. Impacts of the ambient temperature

Fig. 18, demonstrates that when the ambient temperature increases from 26 °C to 36 °C, the outlet air temperature and specific humidity both increase. The impacts of the ambient temperature on those two parameters are similar to that in sub-section 4.1.1. However, the difference is the heat pump supplement system provides cooling loads to the solution via the evaporator which can further reduce the working temperature of the solution. The outlet air temperature and specific heat

Fig. 17. Real-time performance of the non-compressive cooling cycle (T_{abs} = 35 °C, T_{des} = 30 °C, RH_{air} = 80%, X_{sol} = 62%, T_{amb} = 30 °C, m_{air} = 0.03 kg/s).
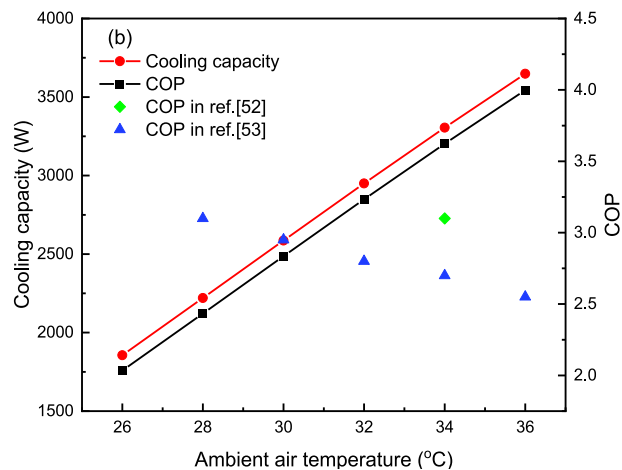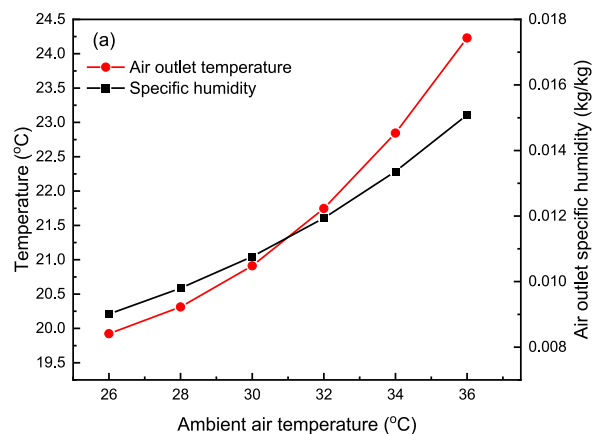
Fig. 18. The impacts of the ambient temperature on performance and comparison with published results (RH_{air} = 80%, X_{sol} = 62%, B_{ch} = 0.1, m_{air} = 0.07 kg/s B_{dch} = 0.57, $Q_{eva + chi}$ = 3 kW).

of the heat pump supplement system are only 20.9 °C and 0.0107 kg/kg which are lower by 25% and 26.7% respectively, compared to those in the above non-compressive system mentioned in section 4.1.1 when the operating conditions are the same. The cooling capacity of the system also increases from 1855W to 3648W due to the higher temperature and water vapour partial pressure between the solution and air in the humidifier. As the heat pump system does not interact with ambient air, the compressor power consumption does not change during the variation of the ambient temperature. Hence, the COP of the proposed system increases with the increased cooling capacity. By comparing to the previously published results in ref (Subiantoro et al., 2014), the COP of the proposed system improved by 16.9% when the ambient air temperature is 34 °C. Meanwhile, similar improvement can be observed when compared to the results in ref (Pino et al., 2015). when the ambient air is over 32 °C and the set cabin temperature is 21.25 °C. However, it should be noted that the COP of the proposed system starts lower than the COP in Ref (Pino et al., 2015). when the ambient temperature is lower than 30 °C. This can be explained from two aspects. First, on the condenser side of the reference air conditioning system, the refrigerant in the condenser transfers heat to the ambient air, and the condensing pressure decreases as the ambient air temperature decreases, resulting in a reduction in compressor power consumption. Second, the intake air in the reference is only 30% of the air mass flow, which is lower than the fresh air mass flow in the proposed system. However, the performance disadvantage of the proposed system at non-high temperature conditions can be compensated by the non-compressive cooling system mentioned above.

4.2.2. Impacts of the battery discharging C rate

As shown in Fig. 19, the battery discharging C rate also has a significant influence on the performance of the proposed system. In Fig. 19 (a), when the battery discharging C rate increases from 0.45C to 0.66C, the outlet air temperature and the specific humidity decrease by 9.1% and 3% respectively. This is because, when the battery discharging C rate increases, the waste heat through the chiller also increases. As the battery coolant inlet and outlet temperature of the chiller are set as constant, the evaporating temperature is reduced in order to increase the LMTD in the chiller. Meanwhile, as the heat transfer rate in the chiller and evaporator is constant, the mass flow rate of the solution also decreases in order to compensate for the increasing LMTD and reduce the heat transfer rate in the evaporator to maintain the energy conversion. Due to the decrease in the solution mass flow rate, the solution working temperature decreases correspondingly, although the total cooling capacity provided by the evaporator and MH is reduced. The solution with a lower temperature in the dehumidifier enhances the temperature difference between the air side and solution side resulting in a higher heat and mass transfer coefficient according to Eqs. (14) and (17). Fig. 19(b) reflects the relationship between the cooling capacity, COP, and battery discharging C rate. The cooling capacity and COP increase by 7.9% and 4.3% respectively when the battery discharging C rate varies from 0.45C to 0.66C. Due to the unchangeable air mass flow rate which leads to the lower outlet air temperature and specific humidity, the cooling capacity increases with the increasing battery discharging C rate. Although the increasing battery discharging C rate leads to a decrease in evaporating temperature, resulting in a higher compressing ratio and compressor higher power consumption based on Eq. (33), the increased ratio in cooling capacity is much higher. Therefore, according to Eq. (35), the COP increases with the increasing battery discharging C rate. However, the increased speed of the COP gradually decreases in this process which is because the decreases in outlet air specific humidity gradually slow down and tend to be constant at a high battery discharging C rate. Furthermore, the faster-reducing speed of evaporating temperature due to the lower refrigerant mass flow rate caused by increasing heat of evaporation maybe also be a contributing reason.
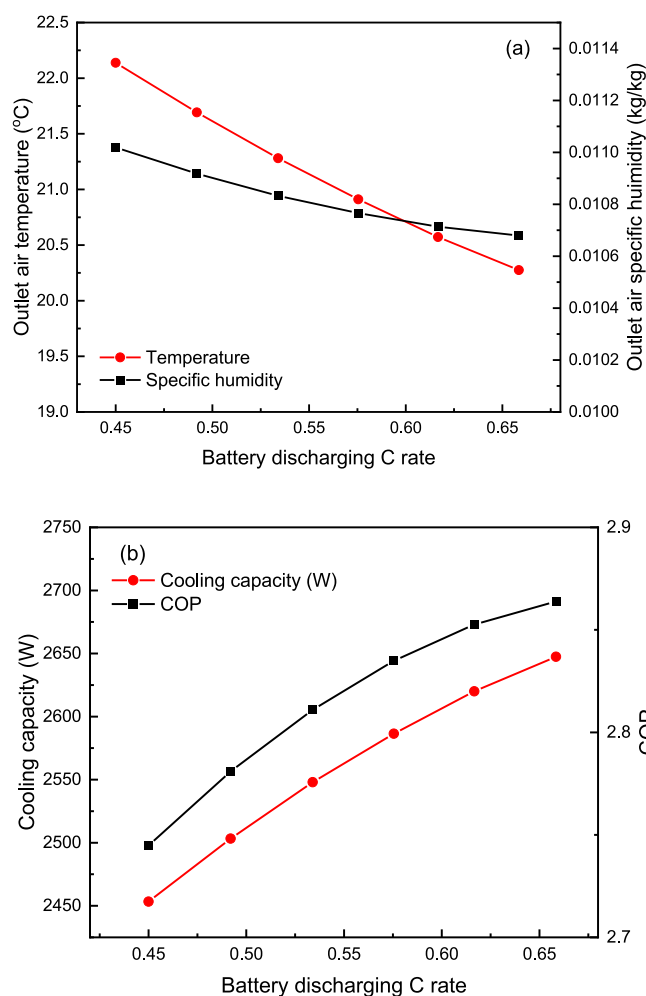
Fig. 19. Impact of the battery discharging C rate on performance ($RH_{air} = 80\%$, $X_{sol} = 62\%$, $B_{ch} = 0.1$, $m_{air} = 0.07$ kg/s, $T_{amb} = 30$ °C, $Q_{eva + chi} = 3$ kW, $B_{ch} = 0.1$).

4.2.3. Impacts of the battery charging C rate

Fig. 20 describes the influence of battery charging C rate on the performance of the proposed heat pump supplement, open-metal hydride system assisted cooling, and dehumidification system. In the proposed cases, the impacts of the battery charging C rate are lower due to the introduced heat pump complement compared to the non-compressive system mentioned in section 4.1.2. With the battery charging C rate increasing from 0.054 to 0.0182, the outlet air temperature only declines by 0.7 °C, from 21.3 °C to 20.6 °C. Additionally, the dehumidification ability also increases marginally, which leads to the outlet air specific humidity decreasing by 3.8%. The reason for this is that when the battery charging C rate increases, the required hydrogen mass flow rate discharged by MH increases correspondingly and increases the cooling capacity supplied by the open metal hydride system. As a result, the solution temperature out of the open metal-hydride system decreases. However, due to the pinch point limits of the evaporator, the mass flow rate of the solution increases and leads to a stable solution working temperature according to Eq. (29)–(31). Hence, the increasing solution mass flow rate increases the average vapour partial pressure and temperature of the solution inside the humidifier and enhances the heat and mass transfer inside the dehumidifier and leading to an increased cooling capacity. The COP also increases by 5% when the battery charging C rate changes from 0.054C to 0.182C. This is because the battery waste heat does not increase, so the compressor power consumption can be seen as constant which leads to an increase in the
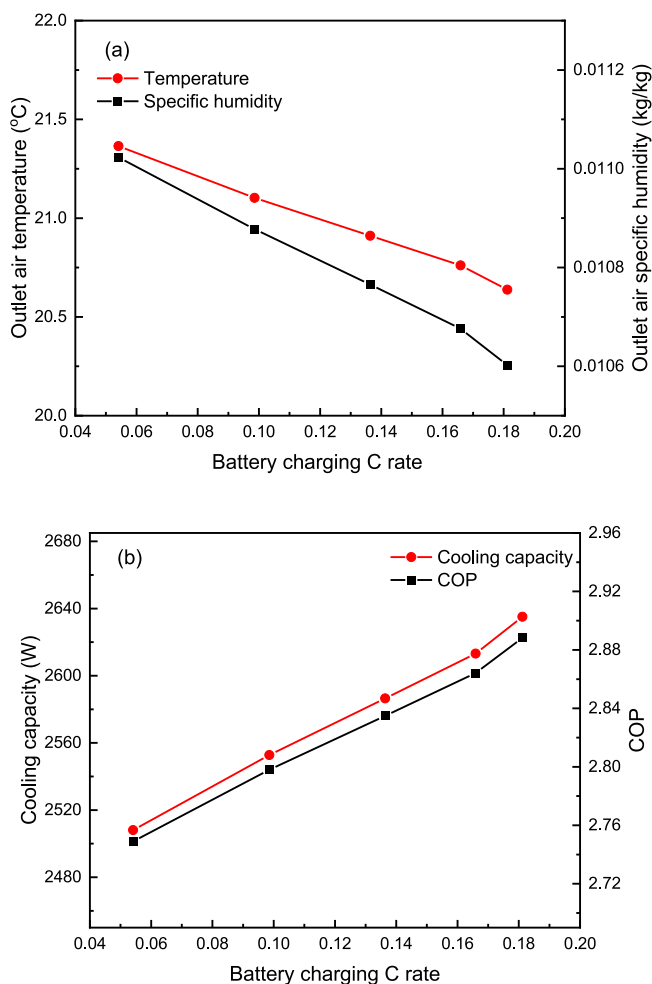
Fig. 20. Impacts of the battery charging C rate on performance ($RH_{air} = 80\%$, $X_{sol} = 62\%$, $B_{ch} = 0.1$, $m_{air} = 0.07$ kg/s, $T_{amb} = 30$ °C, $Q_{eva} = 1.7$ kW, $B_{dch} = 0.1$, $Q_{chi} = 1.3$ kW).

COP with the help of the increased cooling capacity.

4.2.4. Real time performance

Fig. 21 shows the real-time performance of the proposed open-metal
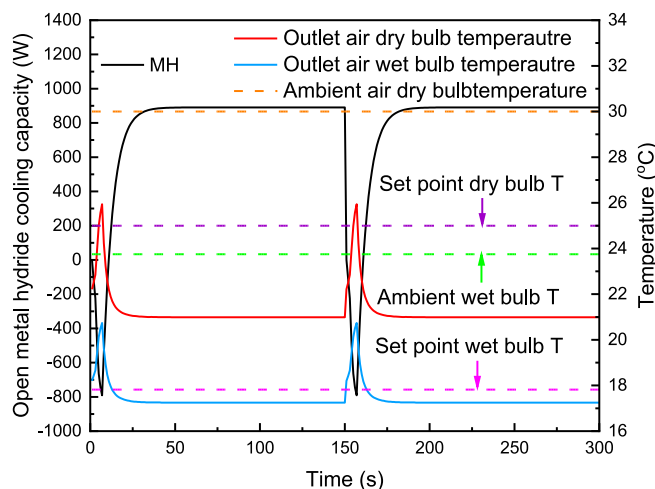
Fig. 21. Real-time performance of the non-compressive cooling cycle ($T_{abs} = 35$ °C, $T_{des} = 30$ °C, $RH_{air} = 80\%$, $X_{sol} = 62\%$, $T_{amb} = 30$ °C, $m_{air} = 0.07$ kg/s).

hydride-assisted, heat pump-supplemented cooling and dehumidification system. The results show that the proposed system can substantially improve performance, especially during the metal hydride transition stage. The maximum outlet air temperature is lower than the supply air temperature in a non-compressive system and far lower than the ambient temperature even with an air mass flow rate of 0.07 kg/s which is the maximum air mass flow rate mentioned in Ref. (Fojtlin et al., 2016). Although the outlet air temperature was slightly above the cabin set point for a period of 2 and 12 s above the wet bulb temperature set point, this could be improved by increasing the cooling capacity of the evaporator or reducing the mass air flow if the cooling demand is flexible.

In summary, the proposed heat pump supplemented, open metal hydride-assisted, cooling and dehumidification system has better performance under high temperature and high humidity conditions compared to the previously published results in Ref. (Subiantoro et al., 2014; Pino et al., 2015). In particular, the COP can be improved by 64% at an ambient temperature of 36 °C, however, it starts operating detrimentally when the ambient temperature is lower than 30 °C. This could be solved by switching the heat pump supplemental mode and non-compressive model alternatively as the non-compressive cooling mode can provide sufficient cooling capacity without the compressor power consumption and increase the overall system COP. The proposed system is also affected by the battery discharging C rate which performs better under high battery power output conditions. The performance under low power output conditions could be improved by adjusting the battery coolant inlet and outlet temperature. This may have specific effects on the battery temperature uniformity, but the Model Predictive Control (MPC) strategy may minimize the impacts. The performance could be improved with the help of the increasing battery charging C rate, but the improvement is limited by the maximum fuel cell current density.

5. Conclusions and future work

A highly integrated hybrid cooling system for an electric vehicle with a fuel cell extender, open-metal-hydride system, liquid desiccant dehumidification system, and heat pump waste system was proposed. The newly designed system can operate with or without the compressed refrigerant cycle which can improve the COP of the vehicle thermal management system and the cabin comfort in a hot climate. A numerical model was developed and validated by experimental results and published results. According to the results, the following conclusions were drawn.

- Under no-compressive operating mode, the cooling capacity of the proposed system improved by 25%–70% when the battery charging C rate ranged from 0.05 to 0.18, and the improvement slowed down when the charging C rate exceeded 0.1.
- The fluctuations due to the thermal losses during the transition between two MHs caused 12s of the invalid cooling process, during which the proposed system ran under the non-compressive mode.
- The proposed system can achieve better performance with the increase of the ambient temperature while operating in heat pump supplemental mode. The COP increased by 40.9% when the ambient temperature varied from 30 °C to 36 °C.
- The COP of the proposed system under heat pump supplemental mode was 16.7% higher than that of the cited traditional vehicle air conditioning system when the ambient temperature was 34 °C with the same cabin temperature set point of 25 °C
- With the assistance of the heat pump, the proposed system could always provide supply air with a temperature under the setpoint of 24.5 °C, but a 12s insufficient dehumidification period could be observed if the relative humidity of the setpoint was 50%.

Potential future direction of the research

Further research could focus on how to further eliminate the fluctuation during the transition between the two MHs. Additionally, analysis of the performance under each operating mode from an operating vehicle perspective would be beneficial to help understand how much energy could be saved when the vehicle is running under the practical testing cycle. Moreover, the timing for the transition between the two operating modes should be further optimized to find the most efficient solution. Also, the optimal control of the proposed system will be conducted to achieve efficient and optimal performance.

CRediT authorship contribution statement

Nan Zhang: Conceptualization, Methodology, Software, Validation, Formal analysis, Writing – original draft, Writing – review & editing. **Yiji Lu:** Conceptualization, Writing – review & editing, Supervision. **Zhibin Yu:** Conceptualization, Supervision.

Declaration of competing interest

The authors declare that they have no known competing financial interests or personal relationships that could have appeared to influence the work reported in this paper.

Data availability

Data will be made available on request.

Acknowledgements

References

Akbarzadeh, M., Jaguemont, J., Kalogiannis, T., Karimi, D., He, J., Jin, L., et al., 2021. A Novel Liquid Cooling Plate Concept for Thermal Management of Lithium-Ion Batteries in Electric Vehicles. Energy Conversion and Management, p. 231.

Alahmer, A., 2016. Thermal analysis of a direct evaporative cooling system enhancement with desiccant dehumidification for vehicular air conditioning. Appl. Therm. Eng. 98, 1273–1285.

Albayati, I., Ali, R., Calay, R., 2013. Modelling and examining open circuit voltage for PEM fuel cells. J. Electr. Eng. 13, 140–146.

Bridge, D., Dutta, N., Porteous, S., Rouaud, C., Beloe, N., 2013. Use of palliative technologies in minimising HVAC loads and their impact on EV range. In: Vehicle Thermal Management Systems Conference Proceedings (VTMS11). Woodhead Publishing, pp. 251–265.

Chen, X., Su, Y., Aydin, D., Bai, H., Jarimi, H., Zhang, X., et al., 2018. Experimental investigation of a polymer hollow fibre integrated liquid desiccant dehumidification system with aqueous potassium formate solution. Appl. Therm. Eng. 142, 632–643.

Chen, X., Zhang, N., Su, Y., Aydin, D., Zheng, H., Bai, H., et al., 2019. Performance analysis and design implementation of a novel polymer hollow fiber liquid desiccant dehumidifier with aqueous potassium formate. Therm. Sci. Eng. Prog. 13, 100366.

COP 26 in Glasgow. Int. J. Refrig. 132, 2021 (v-vi).

Crabtree, G., 2019. The coming electric vehicle transformation. Science 366, 422–424.

Cuevas, C., Fonseca, N., Lemort, V., 2012. Automotive electric scroll compressor: testing and modeling. Int. J. Refrig. 35, 841–849.

Davids, M.W., Lototskyy, M., Malinowski, M., van Schalkwyk, D., Parsons, A., Pasupathi, S., et al., 2019. Metal hydride hydrogen storage tank for light fuel cell vehicle. Int. J. Hydrogen Energy 44, 29263–29272.

Deng, L., Li, S., Tang, X., Yang, K., Lin, X., 2023. Battery thermal- and cabin comfort-aware collaborative energy management for plug-in fuel cell electric vehicles based on the soft actor-critic algorithm. Energy Convers. Manag. 283, 116889.

Di Giorgio, P., Di Ilio, G., Jannelli, E., Conte, F.V., 2022. Innovative battery thermal management system based on hydrogen storage in metal hydrides for fuel cell hybrid electric vehicles. Appl. Energy 315, 118935.

Fang, J., Yin, X., Wang, A., Sun, X., Liu, Y., Cao, F., 2021. Cooling performance enhancement for the automobile transcritical CO2 air conditioning system with various internal heat exchanger effectiveness. Appl. Therm. Eng. 196, 117274.

Farsi, A., Rosen, M.A., 2022. PEM fuel cell-assisted lithium ion battery electric vehicle integrated with an air-based thermal management system. Int. J. Hydrogen Energy 47, 35810–35824.

Fojtlin, M., Planka, M., Fišer, J., Pokorny, J., Jicha, M., 2016. Airflow measurement of the car HVAC unit using hot-wire anemometry. EPJ Web Conf. 114, 02023.

Fumo, N., Goswami, D.Y., 2002. Study of an aqueous lithium chloride desiccant system: air dehumidification and desiccant regeneration. Sol. Energy 72, 351–361.

Gillet, T., Andres, E., El-Bakkali, A., Lemort, V., Rulliere, R., Haberschill, P., 2018. Sleeping evaporator and refrigerant maldistribution: an experimental investigation in an automotive multi-evaporator air-conditioning and battery cooling system. Int. J. Refrig. 90, 119–131.

Guo, J.J., Wu, J.Y., Wang, R.Z., Li, S., 2011. Experimental research and operation optimization of an air-source heat pump water heater. Appl. Energy 88, 4128–4138.

Kambly, K.R., Bradley, T.H., 2014. Estimating the HVAC energy consumption of plug-in electric vehicles. J. Power Sources 259, 117–124.

Kinab, E., Marchio, D., Rivière, P., Zoughaib, A., 2010. Reversible heat pump model for seasonal performance optimization. Energy Build. 42, 2269–2280.

Li, L., Gao, S., Wang, B., Li, C., Wang, Y., Sun, B., et al., 2023. Analysis of cooling and heating characteristics of thermal management system for fuel cell bus. Int. J. Hydrogen Energy 48, 11442–11454.

Liu, G., Ouyang, M., Lu, L., Li, J., Han, X., 2014. Analysis of the heat generation of lithium-ion battery during charging and discharging considering different influencing factors. J. Therm. Anal. Calorim. 116, 1001–1010.

Lototskyy, M., Tolj, I., Klochko, Y., Davids, M.W., Swanepoel, D., Linkov, V., 2020. Metal hydride hydrogen storage tank for fuel cell utility vehicles. Int. J. Hydrogen Energy 45, 7958–7967.

Ma, J., Sun, Y., Zhang, S., Li, J., Li, S., 2022. Experimental study on the performance of vehicle integrated thermal management system for pure electric vehicles. Energy Convers. Manag. 253, 115183.

Mahamud, R., Park, C., 2011. Reciprocating air flow for Li-ion battery thermal management to improve temperature uniformity. J. Power Sources 196, 5685–5696.

Meier, K., Kurtz, C., Weckerle, C., Hubner, M., Bürger, I., 2018. Air-conditioning system for vehicles with on-board hydrogen. Appl. Therm. Eng. 129, 1150–1159.

Melinder, Å., 2007. Thermophysical Properties of Aqueous Solutions Used as Secondary Working Fluids [Doctoral Thesis, Comprehensive Summary]. KTH, Stockholm.

Meng, Z., Zhang, H., Lei, M., Qin, Y., Qiu, J., 2018. Performance of low GWP R1234yf/R134a mixture asa replacement for R134a in automotive air conditioning systems. Int. J. Heat Mass Tran. 116, 362–370.

Pakowski, Z., 2007. Chem. Eng. Res. Des. 85, 1683–1684.

Pino, F.J., Marcos, D., Bordons, C., Rosa, F., 2015. Car air-conditioning considerations on hydrogen consumption in fuel cell and driving limitations. Int. J. Hydrogen Energy 40, 11696–11703.

Robaina, M., Neves, A., 2021. Complete decomposition analysis of CO2 emissions intensity in the transport sector in Europe. Res. Transport. Econ. 90, 101074.

Şefkat, G., Özel, M.A., 2022. Experimental and numerical study of energy and thermal management system for a hydrogen fuel cell-battery hybrid electric vehicle. Energy 238.

Seyed-Ahmadi, M., Erb, B., Simonson, C.J., Besant, R.W., 2009. Transient behavior of run-around heat and moisture exchanger system. Part I: model formulation and verification. Int. J. Heat Mass Tran. 52, 6000–6011.

Subiantoro, A., Ooi, K.T., Stimming, U., 2014. Energy Saving Measures for Automotive Air Conditioning (AC) System in the Tropics.

Tian, Z., Gan, W., Zhang, X., Gu, B., Yang, L., 2018. Investigation on an integrated thermal management system with battery cooling and motor waste heat recovery for electric vehicle. Appl. Therm. Eng. 136, 16–27.

Tian, Z., Gu, B., Gao, W., Zhang, Y., 2020. Performance evaluation of an electric vehicle thermal management system with waste heat recovery. Appl. Therm. Eng. 169.

TRANSPORTATION USDO, 2013. New Car Assessment Program (NCAP) FMVSS NO. 305 Incidant Test.

Vashisht, S., Rakshit, D., 2021. Recent advances and sustainable solutions in automobile air conditioning systems. J. Clean. Prod. 329, 129754.

Weckerle, C., Bürger, I., Linder, M., 2017. Novel reactor design for metal hydride cooling systems. Int. J. Hydrogen Energy 42, 8063–8074.

Weckerle, C., Nasri, M., Hegner, R., Linder, M., Bürger, I., 2019a. A metal hydride air-conditioning system for fuel cell vehicles – performance investigations. Appl. Energy 256, 113957.

Weckerle, C., Bürger, I., Linder, M., 2019b. Numerical optimization of a plate reactor for a metal hydride open cooling process. Int. J. Hydrogen Energy 44, 16862–16876.

Wu, S., Feng, L., Changizian, S., Raeesi, M., Aiedi, H., 2022. Analysis of air conditioning system impact on a fuel cell vehicle performance based on a realistic model under actual urban conditions. Int. J. Hydrogen Energy 47, 25899–25912.

Xie, Y., Yang, P., Qian, Y., Zhang, Y., Li, K., Zhou, Y., 2022. A two-layered eco-cooling control strategy for electric car air conditioning systems with integration of dynamic programming and fuzzy PID. Appl. Therm. Eng. 211, 118488.

Xu, B., Arjmandzadeh, Z., 2023. Parametric study on thermal management system for the range of full (Tesla Model S)/compact-size (Tesla Model 3) electric vehicles. Energy Convers. Manag. 278, 116753.

Xu, J., Zhang, C., Fan, R., Bao, H., Wang, Y., Huang, S., et al., 2020. Modelling and control of vehicle integrated thermal management system of PEM fuel cell vehicle. Energy 199, 117495.

Yan, Y.Y., Lin, T.F., 1999. Evaporation heat transfer and pressure drop of refrigerant R-134a in a plate heat exchanger. J. Heat Tran. 121, 118–127.

Yan, Y.-Y., Lio, H.-C., Lin, T.-F., 1999. Condensation heat transfer and pressure drop of refrigerant R-134a in a plate heat exchanger. Int. J. Heat Mass Tran. 42, 993–1006.

Zhang, L.-Z., 2006. Fabrication of a lithium chloride solution based composite supported liquid membrane and its moisture permeation analysis. J. Membr. Sci. 276, 91–100.

Zhang, L.-Z., 2011. Heat and mass transfer in a randomly packed hollow fiber membrane module: a fractal model approach. Int. J. Heat Mass Tran. 54, 2921–2931.

Zhang, L.Z., Jiang, Y., Zhang, Y.P., 2000. Membrane-based humidity pump: performance and limitations. J. Membr. Sci. 171, 207–216.

Zhang, N., Chen, X., Su, Y., Zheng, H., Ramadan, O., Zhang, X., et al., 2019a. Numerical investigations and performance comparisons of a novel cross-flow hollow fiber integrated liquid desiccant dehumidification system. Energy 182, 1115–1131.

Zhang, J., Kærn, M.R., Ommen, T., Elmegaard, B., Haglind, F., 2019b. Condensation heat transfer and pressure drop characteristics of R134a, R1234ze(E), R245fa and R1233zd(E) in a plate heat exchanger. Int. J. Heat Mass Tran. 128, 136–149.

Zhang, N., Lu, Y., Kadam, S., Yu, Z., 2023. Investigation of the integrated fuel cell, battery, and heat pump energy systems. Energy Convers. Manag. 276, 116503.

Zou, H., Jiang, B., Wang, Q., Tian, C., Yan, Y., 2014. Performance analysis of a heat pump air conditioning system coupling with battery cooling for electric vehicles. Energy Proc. 61, 891–894.